CFD based Investigations for the Design of Severe Service Control Valves used in Energy Systems

Taimoor Asim[*1] Matthew Charlton [2] Rakesh Mishra[3]

[1,3] School of Computing & Engineering

University of Huddersfield, Queensgate, Huddersfield HD1 3DH, UK

[2] Weir Valves & Controls UK Ltd, Britannia House, Elland HX5 9JR, UK

[1]t.asim@hud.ac.uk, [2]Matthew.Charlton@weirgroup.com [3]r.mishra@hud.ac.uk

Abstract

Multistage severe service control valves are extensively used in various energy systems, such as oil & gas, nuclear etc. The primary purpose of such valves is to control the amount of fluid flow passing through them under extreme pressure changes. As opposed to the conventional valves (butterfly, gate etc.), control valves are often installed in energy systems with geometrically complex trims, comprising of various geometrical features, formed by a complex arrangement of cylindrical arrays. The pressure within the trim varies in controlled steps and hence, cavitation resistance can be embedded in the trim through improved design process for the trim for severe service applications in energy systems. The flow characteristics within a control valve are quite complex, owing to complex geometrical features inherent in such designs, which makes it extremely difficult to isolate and quantify contribution of these features on the flow characteristics. One of the most important design parameters of such trims is the flow coefficient (also known as flow capacity) of the trim which depends on the geometrical features of the trim. The design of valves for particular performance envelop within the energy systems depends on effects of complex trim geometrical features on performance characteristics; hence, the focus of recent research is on quantifying the hydrodynamic behaviour of severe service control valves, including the trims. This includes the estimation of the local flow capacity contributions of the geometrical features of the trim through detailed numerical investigations. In this work, a tool has been developed that can be used to predict the local contribution of geometrical features on the flow coefficient of the trim. It is expected that this work will result in better performance of the energy systems where these valves are used.

Keywords: Computational Fluid Dynamics (CFD), Severe Service, Control Valves, Flow Capacity, Energy Systems

1.0   Introduction

Valves are an integral part of any piping network and are used in a variety of industries for various process control applications. The design of valves is a specialist area and the performance of valves is integral to the performance of the energy systems. The severe service control vales typically have very complex flow paths and it is necessary to have understanding of flow characteristics through the complex pathways to eliminate undesirable effects such as vibrations, noise and cavitation in energy systems. The designs of such valves are carried out with the help of well-known standards but many times undesirable local flow effects cannot be eliminated through such designs. The standards are continuously updated to incorporate state of the art knowledge into the design process through extensive experimental and numerical research work carried out all over the world. Newer designs are continuously

---

[*] Corresponding Author

Tel.: +44 1484 472323

being developed for energy systems for which design methods illustrated in standards may be only partially applicable. In such cases a thorough fluid dynamic analysis is necessary to design such valves. The performance of the energy system depends on placement of the valve in the loop and fittings around it. Kang et al [1] have carried out both experimental and numerical investigations on the effects of using various pipe configurations/fittings, downstream the control valve, on the flow capacity of the valve. L, T, Y and + type configurations have been used in these investigations. It has been reported that with the use of such fittings, the pressure losses are around 10% more than with no fitting/s attached thus affecting the valve's performance drastically. It has also been observed that the numerical simulations over-predict the flow coefficient of the control valve by 3-5%, as compared to the experimental findings. The measurement accuracy for the valve's flow coefficient was estimated to be ±10%. Limited information regarding the numerical modelling has been provided by the authors, hence, detailed commentary on the reasons for these variations is not possible. Furthermore, the flow capacity recorded is for the whole valve system (including its components), and local variations and contributions to the flow coefficient by various geometric features have not been discussed. Beune et al [2] have also carried out both numerical and experimental investigations on the discharge capacity of high-pressure safety valves. Fluid-structure interaction based numerical techniques have been used to analyse the performance of the valve. A cavitation model, based on Rayleigh-Plesset equation, has been developed and implemented in the numerical solver, assuming no-slip velocity condition between the phases. It has been demonstrated that the experimental results match well with the numerical results when the cavitation model is implemented.

Lin et al [3] carried out detailed numerical investigations on the drag, lift, moment and discharge coefficients, and the hydrodynamic forces acting on a butterfly valve for various Valve Opening Positions (VOPs). It has been shown that SST-kω turbulence model best predicts the flow behaviour within the valve, along-with 2nd order upwind discretisation schemes. It has been reported that the Computational Fluid Dynamics (CFD) based predicted coefficients and forces are in close agreement with the experimental results. Yang et al [4] have carried out detailed numerical investigations on a stop valve, and have reported the complex flow structure within the valves. Wake induced vibrations for various valve geometries have been shown to affect the valve geometry differently, with the low frequency properties of the fluctuating pressure source being the main source of vibrations, both within the pipe and the valve. Limited information regarding the effects of geometrical features on the performance of the valve has been reported. Furthermore, An et al [5] has reported almost linear increase in the flow capacity of a control valve as the valve opening position increases. The flow capacity recorded corresponds to the whole valve system (including its components). The information regarding individual contributions of these components to the global flow coefficient of the valve system has not been discussed. Moreover, Grace et al [6] have developed a parametric equation to predict the flow capacity of choke valve trims, based on upstream geometric parameters. However, this model is most effective when the trim consists of only a small number of ports. Again, the effects of various valve system components on its flow coefficient have not been discussed. Unlike the simplified flow geometry mentioned in An et al [5], sever service valves have a fairly complex geometry. The flow field inside such valves is largely unknown. The experimental studies [7] have been used to predict global performance parameters, such as flow capacity, but interrelation between the geometry and the local flow field is largely unknown. This may causes uncertainty with regards to the performance of the valves in safety critical applications such as energy systems.

Li et al [8] developed a transient CFD based model to predict the hydraulics of a rectangular full open valve tray (trim). 3D two-phase flow of gas and liquid has been analysed to develop a new correlation of liquid hold-up. Interphase momentum transfer term has also been calculated. It has been reported that CFD can be used as an effective tool in the design and analysis of industrial trays. Wu et al [9] carried out numerical investigations on the flow-pressure characteristics of a pressure control valve for automotive fuel supply system. It has been shown that as the valve opening increases, the flow coefficient also increases. Detailed investigations on the effects of various valve system components, on its flow capacity, have not been carried out. Qian et al [10] carried out numerical investigations on the dynamic flow behaviour of a pilot-control globe valve. It has been reported that the internal flow field of the valve is quite complex. Forces and displacements of the valve core have been recorded and analysed at a given operating condition. Valdes et al [11] presented a methodology for development of reduced order models that can be used to estimate the fluid flow and the flow forces in hydraulic valves, as a function of reduced number of critical dimensions and material properties. The methodology developed is based on incompressible flow and makes use of CFD simulations in order to determine the flow resistance coefficient. The developed model can be used to determine the effects of varying geometry on valve's performance. However, the primary limitation of the developed model is that it is applicable to only those kinds of valves in which the flow fields are similar to the valve used by Valdes.

Srikanth et al [12] carried out numerical investigations on compressible flow in a typical puffer type chamber. It has been observed that the velocity vectors in the middle plane of the chamber depict swirling flow characteristics, with turbulent eddies. Static pressure on the same plane has been noticed to be highly fluctuating indicating highly complex flow charcateritics within internals of valves. Amirante et al [13-15] carried out a series of numerical investigations on the flow forces acting on a hydraulic directional control valve. Investigations carried out at various flow rates indicate that the maximum flow force occurs when the recirculation flow rate vanishes. Moreover, the peak value of the flow force increases with increasing flow rate, but its position remains fixed. There are however differences in the pressure fluctuations due to the geometrical effects. Lisowski et al [16-18] carried out a series of numerical investigations on the flow characteristics of a proportional flow control valve. CFD based predictions on the pressure losses within the valve have been shown to be within ±5% band as compared to the experimentally obtained data. CFD based predictions have been used to generate new design features for better hydraulic efficiency of the valves.

Critical analyses of the published literature regarding the flow behaviour and the flow capacity analysis of severe service control valves reveal that these analyses are carried out mostly on the global performance parameters of the valve, such as the flow capacity of the control valve system (valve and its components together). However, a better understanding of the local flow phenomena and local flow capacity of the different components of the control valve system is extremely important in order to ensure better performance characteristics during routine as well as safety critical applications in energy systems. In case of severe service control valves, one of the most important components of the system is the trim. In the present study, local flow field analyses within a trim has been carried out at various control valve opening positions, in order to estimate the contribution of various geometrical features of the trim on its local flow capacity. Furthermore, the contributions from other valve components, such as the valve body and the seat, have also been enumerated. A combination of experimental and numerical investigations has been carried out to achieve this. In the next section, the details of the methodology to calculate the flow capacity (global) of the

components of the control valve system (valve, seat and trim) have been discussed, extending it further to calculate the local flow capacity within the trim.

2.0   Flow capacity of a severe service control valve system

A control valve system comprises of three main components through which flow takes place i.e. the valve body, the seat and the trim, as shown in figure 1 [19]. The control valve systems are installed within severe service (high differential pressure) pipelines. The flow enters the valve system via the inlet section of the system. The flow then enters the trim, which in the present study, consists of stacks/layers (called disks) of staggered cylindrical columns, offering resistance to the flow. Hence, the fluid pressure drops in steps. Upon exiting the trim, the flow enters the outlet section of the valve system, from where it propagates to the outlet duct/pipe. The amount of flow passing through the control valve system is controlled by an actuator. The actuator is connected to the stem which moves up and down the central void section of the trim in order to open or close the control valve system to a prescribed valve opening position.
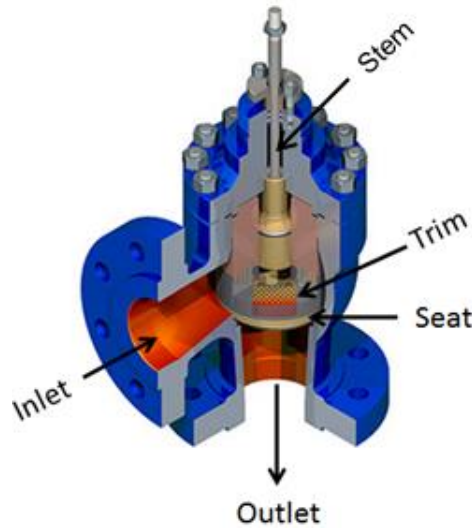
Figure 1 Components of a Severe Service Control Valve [19]

The design of a control valve system is dependent on the requirements of the flow coefficient of the system, which can be computed as [20]:

$$Cv_{Control-Valve-System} = \frac{1}{\sqrt{\left(\frac{1}{Cv_{Valve\,Body}^2}\right)+\left(\frac{1}{Cv_{Seat}^2}\right)+\left(\frac{1}{Cv_{Trim}^2}\right)}} \tag{1}$$

The structure of equation (1) is indicative of flow in series along the components of the control valve system. The methodology to calculate the flow capacity of the severe service control valve system has been extensively reported in the British Standard EN 60534-2-3 and International Electrotechnical Commission 60534-2-3. These standards describe the sizing equation for the non-choked, incompressible fluid flow in a severe service control valve as [20-21]:

$$Q = N_1 F_R F_P Cv_{Control-Valve-System} \sqrt{\frac{\Delta P}{\frac{\rho}{\rho_o}}} \tag{2}$$

where Q is the volumetric flow rate of the fluid passing through the control valve system, N_1 is a numerical constant, F_R is the Reynolds number factor, F_P is piping geometry factor, $Cv_{Control\text{-}Valve\text{-}System}$ is the flow capacity of the system, ΔP is the differential pressure across the control valve system, ρ is the density of the fluid flowing in the control valve system and ρ_o is the density of water. The value of N_1 depends on the units used to compute equation (1). If the volumetric flow rate is measured in m^3/hr and the differential pressure is measured in kPa, the value of N_1 is 0.0865 [7]. The value of F_R depends on whether the flow within the valve is laminar or turbulent; for turbulent flows, its value is 1. The value of F_P depends on whether any pipe fittings (such as a reducer, expander etc.) is attached to the valve. In case there are no pipe fittings attached to the valve, the value of F_P is 1. ρ/ρ_o is the specific gravity of the fluid, and for flow of water within the valve, its value is 1.

It has been mentioned in [21] that with the exception of valves with very small values of $Cv_{Control\text{-}Valve\text{-}System}$, turbulent flow will always exist. It has been observed, while conducting experiments in the present study, that $Cv_{Control\text{-}Valve\text{-}System}$ values are not very small, and hence turbulent flow assumption seems reasonable, i.e. $F_R=1$. Furthermore, there has been no pipe fitting used with the valve considered in the present study, hence the value of F_P is 1. Based on the units used for Q and ΔP in the present study (m^3/hr and kPa), and the working fluid (water), equation (2) can be re-written as [20]:

$$Cv_{Control-Valve-System} = \frac{11.56\,Q}{\sqrt{\Delta P}} \tag{3}$$

It can be noticed from equation (3) that the flow capacity of the control valve system is directly proportional to the volumetric flow rate through the system and inversely proportional to the square root of the differential pressure across the system. These values can be measured both experimentally and numerically. It is noteworthy at this point that equation (3) is valid only for Newtonian fluids and for non-vaporizing conditions.

The flow capacity of the valve body and the seat can be computed, for the valve considered in the present study, as [21]:

$$Cv_{Valve-Body} = k_1 \left(\frac{D_{Valve}}{D_{Seat}}\right)^2 \tag{4}$$

and,

$$Cv_{Seat} = k_2 \left(\frac{D_{Valve}}{D_{Seat}}\right)^2 \tag{5}$$

where k_1 and k_2 are coefficients that depend on the geometry of the valve and the seat. Equations (4-5) have been developed based on CFD analyses of flow though these components. As the flow field through these components is reasonably simple, the focus of further investigations is towards the flow distribution within the trim. The flow coefficient of the trim (Cv_{Trim}) in equation (1) can then be computed as:

$$Cv_{Trim} = \frac{1}{\sqrt{\left(\frac{1}{\left(\frac{11.56\,Q}{\sqrt{\Delta P}}\right)^2}\right) - \left(\frac{1}{\left(k_1\left(\frac{D_{Valve}}{D_{Seat}}\right)^2\right)^2}\right) - \left(\frac{1}{\left(k_2\left(\frac{D_{Valve}}{D_{Seat}}\right)^2\right)^2}\right)}} \tag{6}$$

It should be noted that Cv_{Trim} in equation (6) is the global flow capacity of the trim i.e. across the whole trim, which can be determined both experimentally and numerically.

It can be seen in equations (4-5) that the flow capacities of the valve body and the seat depend on their geometrical features, which is also true for the trim. However, the interdependence of trim's local flow capacity and its geometrical features cannot be established using conventional experimental methods. Hence, in the present study, this interdependence has been established with the use of CFD based techniques. Firstly, the global flow capacity of the trim has been measured experimentally. This is then compared against the CFD predictions of the same. Then, in-depth analysis of the local flow capacity of the trim, and various geometrical features of the trim, and at various valve opening positions, has been carried out.

3.0.   Estimation of global flow capacity of the trim

In order to determine Cv_{Trim} in equation (6), detailed experimental investigations have been carried out in the present study. The flow capacity of the valve and the seat are known (based on their diameters), and hence only $Cv_{Control-Valve-System}$ needs to be computed experimentally to determine Cv_{Trim}.

In accordance with BS EN 60534-2-5 [22], the test setup has been constructed, comprising of two straight lengths of pipe, connected to the ends of the valve, as shown in figure 2. The upstream pipe is 20 times longer than the nominal diameter of the pipe (d) while the upstream pressure tapings are attached at a distance of 2 * nominal diameter of the pipe, from the inlet of the valve. The downstream pipe is 7 times longer than the nominal diameter of the pipe while the downstream pressure tapings are attached at a distance of 6 * nominal diameter of the pipe, from the outlet of the valve. The nominal diameter of the pipeline is 100mm.
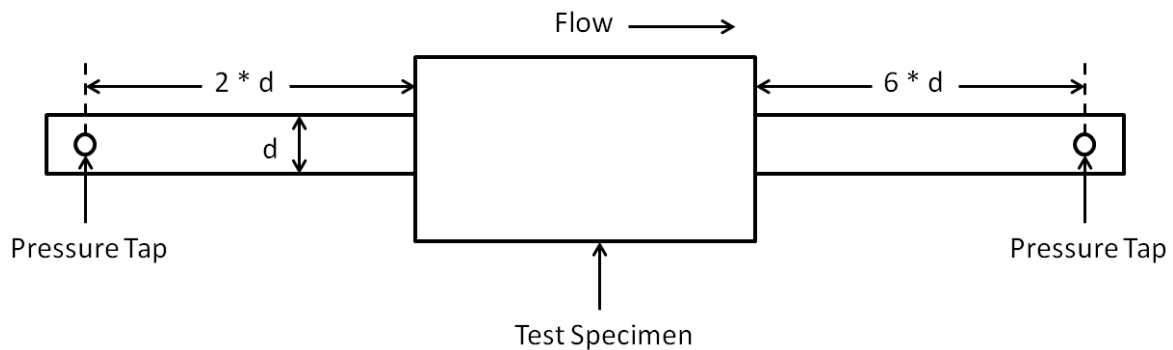
Figure 2 Dimensions of Upstream and Downstream sections

Clean mains water is supplied to the centrifugal pump from the water storage tank, once the upstream ball valve is opened. A turbine flow meter is positioned downstream of the pump, and upstream of the test valve, to monitor flow rate. The pressure taps of the pipeline are connected to a compact liquid differential pressure transducer in order to record the pressure drop between the upstream and downstream pressure tap locations. The differential pressure transducer measures differential pressure of upto 2.5bar, with an accuracy of ±0.5% (IEC60770). The output signal of the transducer is transmitted over a linear range from 4 to 20mA, which is converted into 0 to 10V using an AC-DC converter. The schematic of the test setup is shown in figure 3.
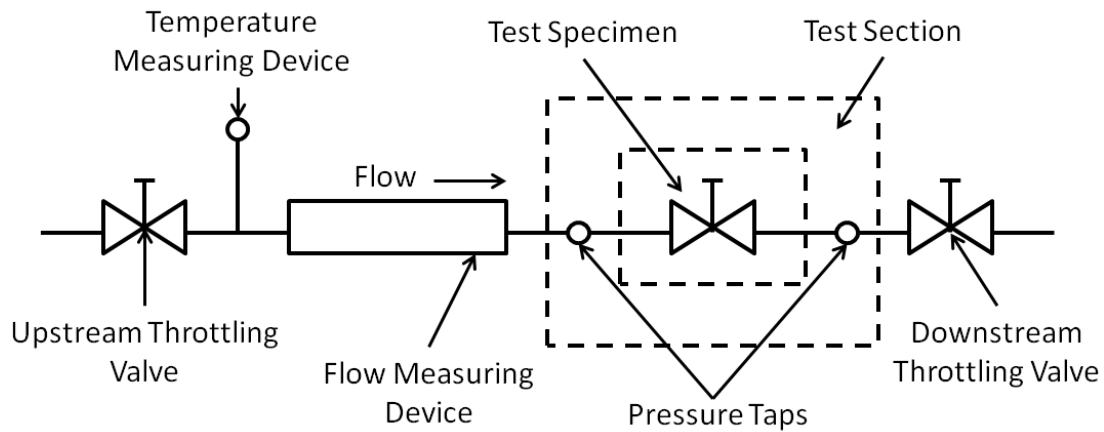
Figure 3 Schematic of the Test Setup

Figures 4 depict the installed flow loop setup for the capacity testing of the valve used in the present study. The actuator sitting on the top of the valve is connected to a loop calibrator, which is further connected to a compressed air supply maintained at 4bar gauge. The loop calibrator is used to control the valve opening position. The loop calibrator has built-in 24V DC power supply and measures $0 - 24$mA DC current, with an accuracy of 0.01%. It can be further seen in figure 4 that four pressure tapings have been connected at both upstream and downstream locations. These pressure tapings measure the average static gauge pressure at the specified location.
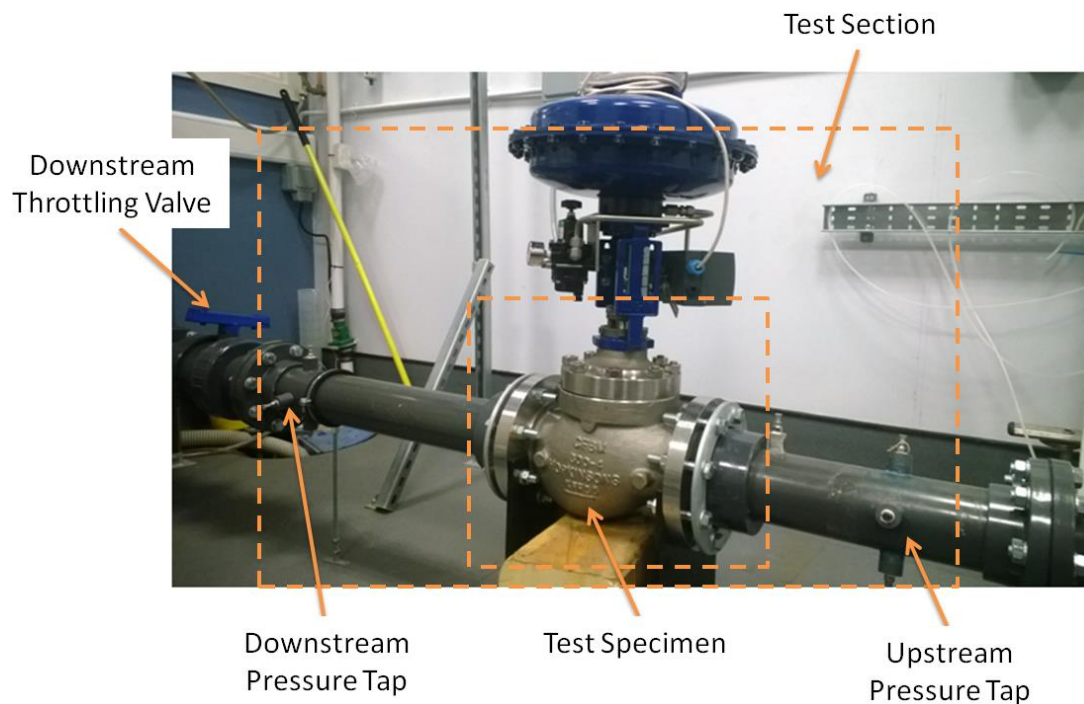
Figure 4 Flow Loop Setup

Test runs have been carried out as per test procedure VT-QC-SP503 [21]. The main objective of the test programme is to determine the flow capacity of the control valve system in equation (3), from which the flow capacity of the trim can be computed as per equation (6). The tests have been conducted at valve opening positions of 100% (fully open), 80%, 60%, 40%, 20% and 10% in order to cover a wide range of operation of the control valve.

The experimental data for the aforementioned test runs is tabulated in table 1. Volumetric flow rate (Q) in ltrs/min and the pressure drop across the valve (ΔP) in volts are recorded at various valve opening positions. The flow rate and pressure drop across the valve are then computed in m^3/hr and kPa units, from which $Cv_{Control-Valve-System}$ is calculated using equation (3). Using known values of $Cv_{Valve-Body}$ and Cv_{Seat}, Cv_{Trim} in equation (6) is computed.

Table 1 Experimental data for Cv_{Trim}

VOP	Q	ΔP	$Cv_{Control-Valve-System}$	$Cv_{Valve-Body}$	Cv_{Seat}	Cv_{Trim}
(%)	(m^3/hr)	(kPa)	$\left(\sqrt{\dfrac{m^7}{kg}}\right)$	$\left(\sqrt{\dfrac{m^7}{kg}}\right)$	$\left(\sqrt{\dfrac{m^7}{kg}}\right)$	$\left(\sqrt{\dfrac{m^7}{kg}}\right)$
100	51.8	342.84	32.3	301.6	65.0	37.5
80	45.9	354.48	28.2	301.6	65.0	31.4
60	36.6	371.28	22.0	301.6	65.0	23.4
40	25.6	378.36	15.2	301.6	65.0	15.7
20	11.1	373.44	6.6	301.6	65.0	6.7
10	7.1	375.00	4.2	301.6	65.0	4.2

It can be seen that at 10% valve opening position, the volumetric flow rate is 7.1m^3/hr, and the differential pressure across the valve is 375kPa, hence, Cv_{Trim} works out to be 4.2. As the VOP increases to 20%, volumetric flow rate and Cv_{Trim} increase to 11.1m^3/hr (56% increase) and 6.7 (59.52% increase) respectively. Further opening the valve to 40% increases the volumetric flow rate and the flow capacity of the trim by 130% and 134% respectively, as compared 10% opening values. Comparing the data between VOPs of 60% and 100% reveals that volumetric flow rate and the flow capacity of the trim increases by 12.85% and 19.43% respectively from VOP of 60% to 100%. It can also be noticed that there are marginal variations within the differential pressure across the valve at all VOPs. Hence, it can be concluded that as the valve opening position increases, the volumetric flow rate across the valve increases, increasing the flow capacity of the trim. This can be further visualised in figure 5.
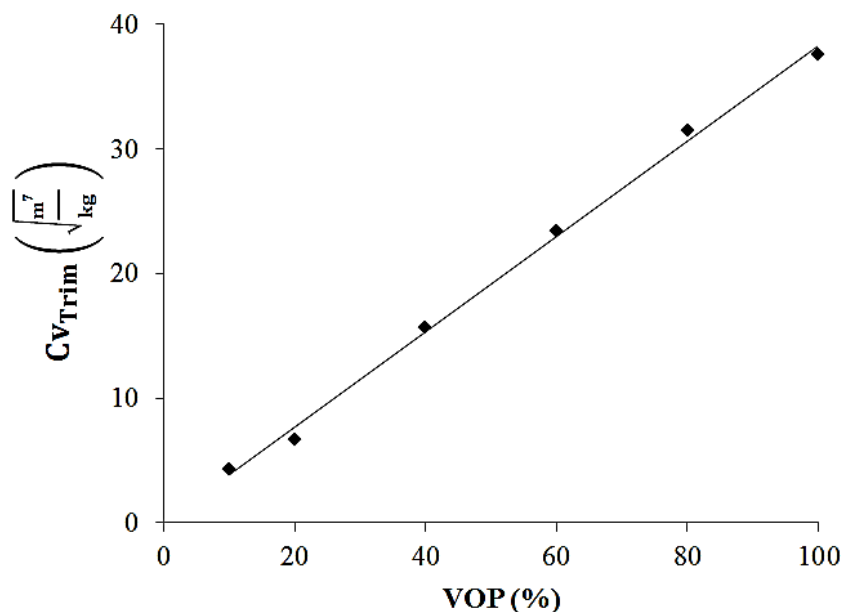
Figure 5 Variations of Cv_{Trim} with valve opening positions

The experimental findings presented here are in-line with the findings in other experimental studies carried out by various investigators [23-24]. However, the primary limitation with the experimental results is that they provide information about global Cv_{Trim} only, and not on the quantitative effects of local geometrical features and their contribution towards overall Cv. This limits the information and the necessary knowledge to be able to optimise the valve geometry for better local as well as global performance characteristics. Computing the local flow capacity within the trim is an intricate task, which is accomplished in the present study by utilising the advanced Computational Fluid Dynamics based numerical techniques. With the recent advancements in computational power, it has become possible to analyse the flow behaviour within very complex geometries (like the one considered in the present study) with reasonable accuracy [25-28]. Hence, the following section/s present the details of the CFD modelling approach employed to locally analyse the capacity of the trim, and quantify local contributions.
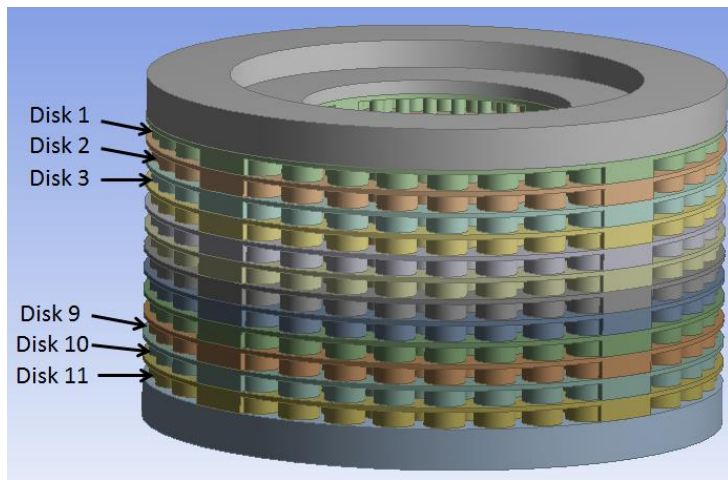
4.0   Local flow capacity of the trim

A trim used in severe service control valves has complex geometrical features. These features interact with the flow field in a complex manner. An attempt has been made here to develop an analytical model to quantify the local flow capacity of the trim based on these geometrical features.

A valve trim is a geometrically complex structure, consisting of stacks of disks, where each disk consists of a number of rows (formed by the cylindrical arrays) and flow paths. The trim used in the present study for analysis is shown in figure 6, where figure 6(a) shows the CAD model of the trim, while figure 6(b) depicts the numerical model of a single disk within the trim. It can be clearly seen that the trim under consideration comprises of 11 disks, where each disk comprises of 5 rows. Each row then comprises of multiple flow paths, which are formed between the cylindrical arrays of the same row. Each row has different number of flow paths i.e. rows 1, 3 and 5 have 7 flow paths, whereas, rows 2 and 4 have 8 flow paths. It is also noteworthy that the end flow paths (FP1 and FP7/8) have different shapes for different rows due to the arrangement of the cylindrical arrays in that row. Hence, it is expected that the end flow paths for different rows will exhibit different flow behaviour.
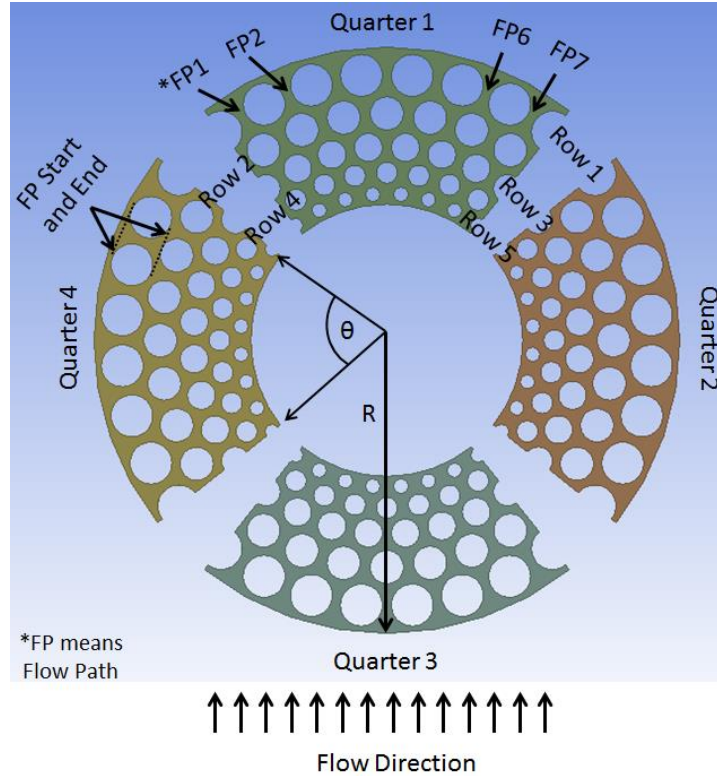

(a)

Figure 6 (a) CAD model of the trim (b) Numerical model of a disk

In order to determine the local flow capacity within a trim, Cv needs to be calculated in disks, rows and flow paths. As a trim consists of a number of disks, where the flow enters each disk simultaneously, the flow capacity of a trim can be computed, in terms of disks, as:

$$Cv_{Trim} = \sum_1^i Cv_{Disk\,i} \qquad (7)$$

where i is the total number of disks in the trim, which in the present study is 11. The structure of equation (7) is typical of the flow in disks in parallel.

Each disk consists of a number of rows, formed by the cylindrical arrays. As the flow propagates through the rows predominantly in radial direction, the flow capacity of the disk, in terms of rows, can be represented as:

$$Cv_{Disk} = \cfrac{1}{\sqrt{\sum_1^j \left(\cfrac{1}{Cv_{Row\,j}^2} \right)}} \qquad (8)$$

where j is the total number of rows, which in the present study is 5. It can be noticed that the structure of equation (8) is that of flow in series.

Each row consists of a number of flow paths through which the flow can take place. The number of flow paths depends on the number of cylinders within that particular row. As the flow enters each flow path of a particular row simultaneously, the flow within flow paths is treated similar to the flow in parallel, and hence, the flow capacity of a row can be represented, in terms of flow paths of that row, as:

$$Cv_{Row} = \Sigma_1^k Cv_{Flow-Path\,k} \qquad (9)$$

where k is the total number of flow paths within that particular row. k is variable in the present study. Its value is 7 for odd number of rows, and 8 for even number of rows. Combining equations (7-9), Cv_{Trim} can be expressed as:

$$Cv_{Trim} = \Sigma_1^i \frac{1}{\sqrt{\Sigma_1^j \left(\frac{1}{\left(\Sigma_1^k Cv_{Flow-Path} \right)^2} \right)}} \qquad (10)$$

$Cv_{Flow-Path}$ in equation (10) can be computed using equation (3), however, the volumetric flow rate (Q) and the differential pressure (ΔP) in that case will be across the flow path, and not the whole trim. Q and ΔP across individual flow paths cannot normally be measured experimentally; hence, the flow capacity of the trim in equation (10) has been computed numerically. CFD based analysis have been carried out in the present study to analyse the flow distribution within the different sections of the trim, which affects the local flow capacity of the trim. Moreover, the effect of VOP on flow distribution has also been analysed in detail.

5.0. Numerical modelling of the control valve

The three dimensional numerical model of the control valve is shown in figure 7(a), where the flow direction is from right to left. The inlet and outlet of the flow domain have been modelled according to the industrial standards, as discussed before (pressure tapping locations). The inlet and outlet pipe sections have been modelled in a different manner than the valve itself, in order to employ different meshing techniques and sizes to the valve and trim surfaces.

The concept of hybrid meshing has been used for meshing the flow domain. The inlet and outlet pipe sections have been meshed using hexahedral elements, while the valve and trim have been meshed with tetrahedral elements. The inlet and outlet pipe sections have been prescribed with a constant mesh element size of 3mm. In order to establish that the results predicted by the numerical solver are independent of the mesh sizing within the test section, three levels of mesh sizing have been used in the present study. Table 2 summarises the mesh sizing within the test section, and also presents the results for mesh independence testing. It can be seen that the test section has been meshed with minimum and maximum sizing of 0.3, 0.5 and 0.7mm, and 3, 5 and 7mm respectively. The mass flow rate predictions suggest that the mesh with the minimum and maximum sizing of 0.3mm and 3mm respectively is capable of predicting the flow variables within the test section with reasonable accuracy, and hence has been chosen for further analysis. This mesh of the flow domain is shown in figure 7.

Three dimensional Navier-Stokes equations, along-with the continuity equation, have been numerically solved in an iterative manner for the turbulent flow of water within the flow domain. As far as the turbulent flow is concerned, two equation Shear Stress Transport (SST) k-ω model has been chosen for turbulence modelling. The primary reason behind choosing SST k-ω model is its superiority in accurately modelling the severe velocity gradients, which are expected to occur within the trims due to complex flow path changes [29-32]. The SST k-ω model includes a blending function for near-wall treatment. It further has the definition of

the turbulent viscosity which is modified to account for the transport of the turbulent shear stress. These features make the SST k-ω model more accurate and reliable for a wider range of flows. Other modifications include the addition of a cross-diffusion term in the ω equation and a blending function to ensure that the model equations behave appropriately in both the near-wall and far-field zones. Further details of SST k-ω model can be found in any turbulence modelling text book [33-35].

Table 2 Summary of mesh sizing and mesh independence testing

Parameters	Level 1	Level 2	Level 3
Minimum size in the test section (mm)	0.3	0.5	0.7
Maximum size in the test section (mm)	3	5	7
Total number of mesh elements (millions)	5.2	3.8	2.2
Mass flow rate across the control valve system (kg/sec)	14.74	14.25	13.17
Difference in mass flow rate w.r.t. Level 1 results (%)		3.32	10.65

(a)   (b)
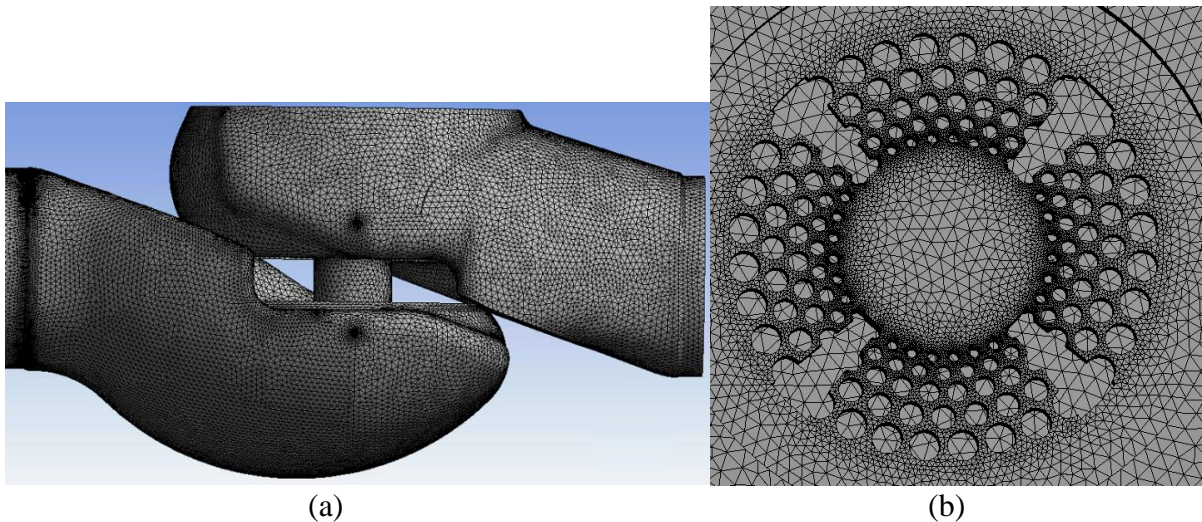
Figure 7 Mesh in (a) the valve (b) the trim

In order to capture the complex flow phenomena associated with the control valve, especially the resolution of the boundary layer flow, mesh layers have been concentrated in the near-wall region, where the boundary layer forms. As it has already been discussed that SST k- ω turbulence modelled has been considered in the present study for modelling turbulence in the flow, the mesh layers have been placed at strategic locations away from the walls. These locations are based on the fact the SST k- ω turbulence model models the viscous sub-layer (i.e. y+ values upto ~5) and the buffer layer (i.e. y+ values from ~5 upto ~12). However, SST k- ω turbulence model resolves the flow in the log-law region (i.e. y+ values from ~12 upto ~300). Hence, the mesh layers are concentrated in the log-law region.

The inlet and outlet boundaries of the flow domain have been specified with total and static gauge pressures respectively. The differential pressure across the control valve has been kept the same as while performing the experiments in the laboratory, which ranges from 341.3kPa

at 100% VOP to 375kPa at 10% VOP. The walls within the flow domain have been modelled as stationary walls with no-slip condition.

5.1.   Verification of CFD results

In order to ascertain the accuracy of the numerical modelling and the solver settings used in the present study, CFD predicted results need to be verified against the experimental findings. In the present study, this has been carried out on Cv_{Trim}, tabulated in table 3. It can be seen that CFD predicted capacity of the trim matches closely with the experimentally calculated Cv_{Trim}. The percentage difference in the two Cv_{Trims}, on average, is 1.6%, most part of which is due to numerical convergence.

Table 3 Benchmarking CFD results

VOP (%)	Experimental Cv_{Trim}	CFD predicted Cv_{Trim}	Percentage difference in CFD predicted Cv_{Trim} w.r.t. Experimental Cv_{Trim}
(%)	$\left(\sqrt{\dfrac{m^7}{kg}}\right)$	$\left(\sqrt{\dfrac{m^7}{kg}}\right)$	(%)
100	37.52	36.29	-3.27
60	23.41	23.61	0.88
40	15.68	16.02	2.17
10	4.24	4.22	-0.33

After it has been established that the CFD predicted results are in close agreement with the experimental findings, detailed qualitative and quantitative analyses on the flow behaviour and the local variations in the capacity of the trim, at various valve opening positions, need to be carried out to understand complex geometry-flow interaction.

Further establishing the superiority of the current numerical modelling approach, a comparative study for the numerical prediction of CV_{Trim} has been carried out. Green et al [27-28] carried out CFD based analysis on the capacity testing of the same trim and the control valve as considered in the present study. The main difference between the two studies is the fact that Green et al considered only one quarter of a single disk for numerical modelling, assuming that the capacity of each quarter of the trim, and each disk of the stack, is the same. However, the CFD based predictions clearly showed significant over-prediction of CV_{Trim} values (56.28 as compared to 36.29 in the current study). Hence, it can be concluded that the numerical modelling approach used in the present study is more accurate in predicting both the trim's and the valve's capacity.

6.0.   Performance analysis of the trim

In order to visualise the flow structure within the trim, figure 8 depicts the velocity vectors within the top disk of the trim at fully open valve position. The velocity vectors shown in the figure corresponds to quarter 1 of the trim as shown in figure 6(b). The flow field corresponding to only one quarter is shown here as it is expected that it will be similar in other quarters of the trim as well. The flow direction through the trim is inwards i.e. through row 1 to row 5, where row 1 corresponds to the largest sized cylinders and row 5 corresponds to the smallest sized cylinders. It can be seen in the figure that as the flow passes through row 1 of the trim, it accelerates to a velocity magnitude of about 12.5m/sec. This increase is expected as the flow area progressively decreases up to the middle section of the cylinders,

resulting in higher flow velocity. The flow velocity can then be seen to decrease to a value of 7.5m/sec, within the same flow path, because of increase in flow area, before entering row 2 of the trim. The flow through row 2 of the trim has same characteristics as noticed in row 1, with the maximum flow velocity magnitude being 11.5m/sec, and the exit flow velocity being 7m/sec. The same features are observed in the flow through rows 3, 4 and 5. However, at the exit of row 5, the flow features are completely different because of different geometrical configurations next to row 5. The above mentioned non-uniformities in the velocity field within the trim increases the hydrodynamic losses within the trim, which is discussed in more detail later [36].

After visualising the flow behaviour within the trim, flow parameters, such as static gauge pressure and velocity magnitude, have been critically analysed for better understanding of the complex nature of flow phenomena within the trim. These parameters uniquely represent the flow capacity through a flow passage and hence can be used later to establish effects of various flow passages on overall flow capacity of the valve. Figure 9 depicts the static gauge pressure variations within the quarter 1 of the top disk of the trim at 100% valve opening position. It can be seen that the pressure is high at the entrance of the trim. The flow then enters the flow path of the 1st row, where, due to area reduction, the static pressure decreases. In the later part of the flow path, as the flow area increases, the static pressure gradually recovers. The flow leaving the 1st row enters the flow path of the 2nd row, where the same phenomenon occurs i.e. area and pressure reduction in the first half of the flow path and vice versa in the later half. The same phenomena repeat in all the rows of the trim, until the fluid leaves the trim. This indicates that the pressure drop occur in a series of steps (equal to the number of rows) as the flow takes place through the trim. Furthermore, it can also been observed that very low pressure regions exist on either sides of a cylinder (more evident in row 5), which is typical of flow taking place over a circular cylinder. Hence, the possible locations within the trim that are more prone to cavitate are the reduced flow areas between the cylinders, where the pressure can locally drop below the liquid vapour pressure of water [37-40].
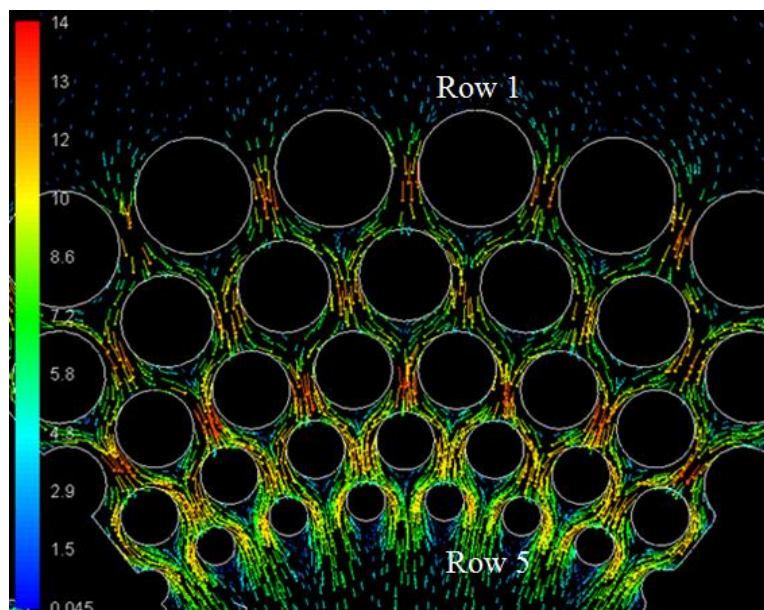
Figure 8 Velocity vectors within quarter 1 of the top disk of the trim at 100% valve opening position

1 In order to further analyse the pressure variations with the trim, figure 10 depicts the local
2 variations in static gauge pressure of the fluid as it passes through the central flow route of
3 the top disk (shown in figure 9). The static pressure has been non-dimensionalised with the
4 dynamic pressure of the fluid within the trim, at the point where maximum flow velocity is
5 achieved. The x-axis corresponds to the radial dimension of the trim, where R is the outer
6 radius of the trim and r is the local radial coordinate where the pressure has been recorded (as
7 shown in figure 6(b)). The vertical dotted lines represent the area between two rows i.e.
8 inclined lines in figure 9.
9
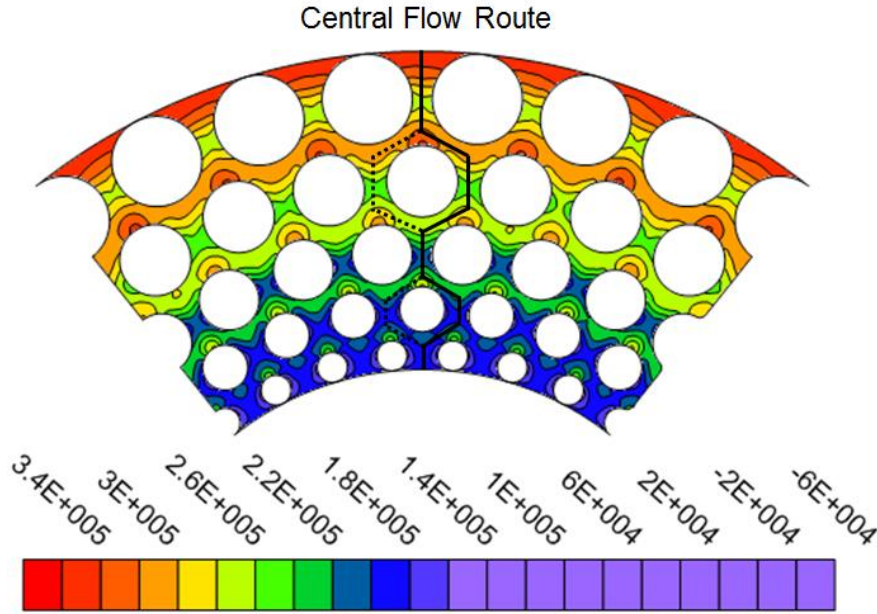
11 Figure 9 Static gauge pressure (Pa) variations within the top disk of the trim at 100% valve
12 opening
13

14 The pressure variations corresponding to the top disk, shown in figure 10, depict that the
15 pressure drops in a series of steps as the fluid flows through the trim. It can be clearly seen
16 that the non-dimensional static pressure at the entry of row 1 is 1.65. As the flow enters the
17 flow path of row 1 i.e. FP R1, due to variations in flow path's area, the pressure first
18 decreases and then increases. At the exit of row 1, the non-dimensional static pressure
19 recovers to 1.5. Between the exit of row 1 and the entry of row 2, the non-dimensional static
20 pressure varies marginally. This is shown through two consecutive vertical dotted lines drawn
21 in figure 10. The same flow phenomenon is seen to occur repetitively until the flow exits the
22 trim. As it has been identified that the pressure variations within flow paths occur due to
23 variations in the flow areas within the flow paths, it is important to establish the interrelation
24 between area change and pressure variations. This has been achieved through a parameter
25 called Flow Area Ratio ($\xi_{n+1/n}$) that has been defined as:
26

$$\xi_{n+1/n} = \frac{\text{Flow Area}_{n+1}}{\text{Flow Area}_n} \tag{11}$$

28

29 where n is the row number. Hence, $\xi_{n+1/n}$ is the ratio of available flow areas between
30 consecutive rows, measured at the middle plane of the cylinders. $\xi_{2/1}$ i.e. effective flow area
31 in row 2 divided by the effective flow area in row 1, is 1.13, which means that the effective
32 flow area in row 2 is 13% more as compared to row 1. Similarly, $\xi_{3/2}$ is 0.89, $\xi_{4/3}$ is 1.21 and
33 $\xi_{5/4}$ is 1.26 respectively. It can be noticed that $\xi_{4/3}$ and $\xi_{5/4}$ are more than 1; however, $\xi_{3/2}$ is

1 less than 1. The effective flow area in row 3 is 11% less than in row 2, and 17% less than in
2 row 4. As the effective flow area in row 3 is less than that in rows 2 and 4, the flow
3 characteristics in the vicinity of row 3 will be different, resulting in higher hydrodynamic
4 losses.
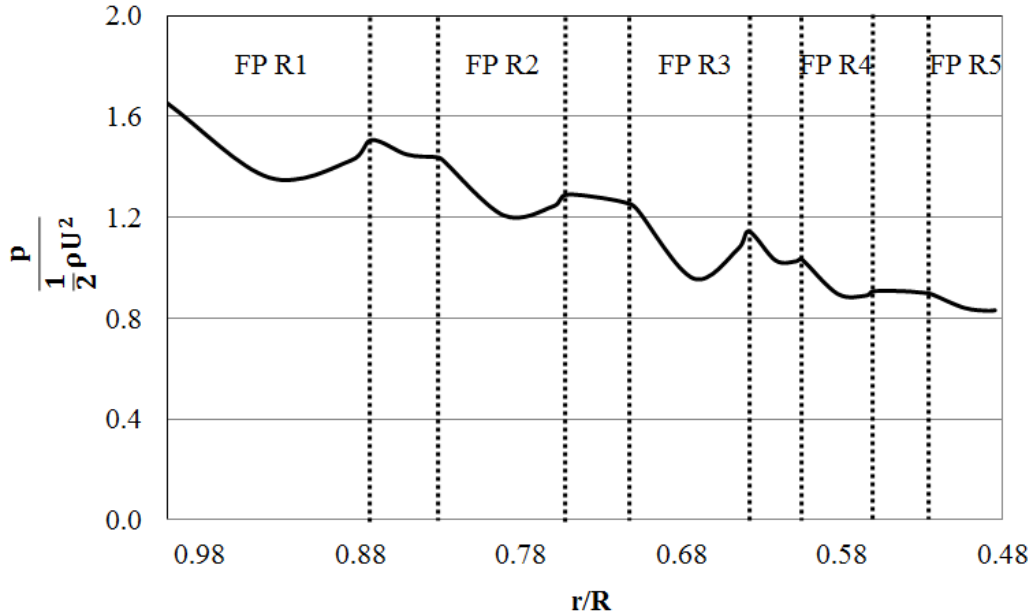
5
6 Figure 10 Normalised static gauge pressure variations along the central flow route within the
7 top disk of the trim at 100% valve opening position
8
9 In order to establish the relationship between flow area ratio and the pressure variations
10 within the trim, non-dimensional differential static pressure, across the flow paths of the top
11 disk, have been plotted in figure 11. It can be seen that, for the top disk, the differential
12 pressure decreases from row 1 to row 2. The same trend is observed from row 2 to row 3,
13 however, from row 3 to row 4, the differential pressure increases, instead of the decreasing
14 trend seen till row 3. From row 4 to row 5, the trend is similar to that observed upto row 3.
15
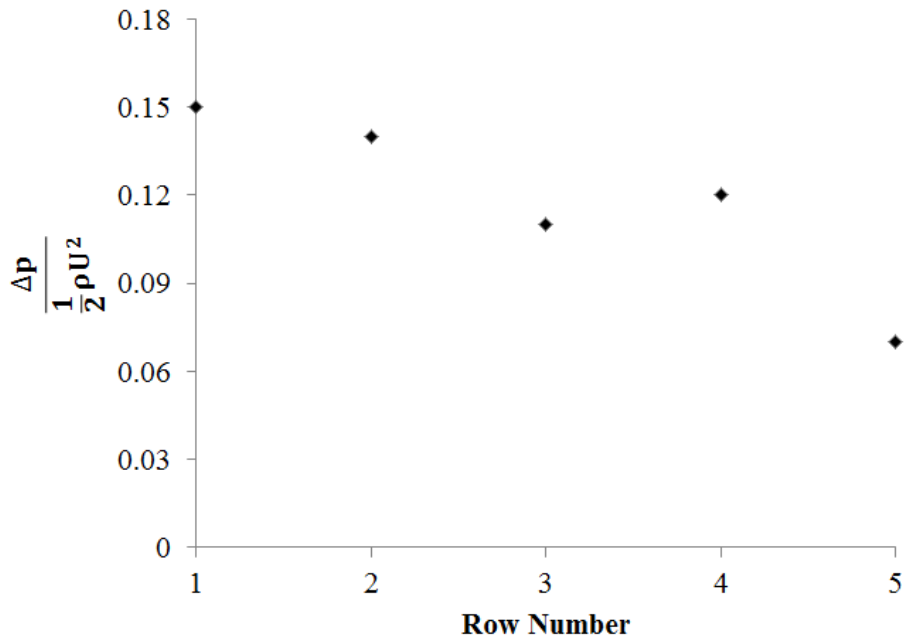
16
17 Figure 11 Normalised differential static gauge pressure variations in the various rows of the
18 trim along the central flow route at 100% valve opening position

After quantitatively analysing the variations in pressure within the trim (for ΔP calculations in equation (6)), variations in the flow velocity magnitude within quarter 1 of the top disk of the trim at 100% valve opening position are depicted in figure 12. The volumetric flow rate calculations in equation (6) are dependent on these variations, hence in order to calculate the flow capacity of the trim, detailed quantitative analysis of the velocity variations is important, and is presented here. It can be clearly seen that the flow velocity magnitude increases in the narrow passages formed between cylindrical arrays within a row. However, continuing from previous discussion, the flow velocity magnitude is highest in the flow paths of the 3rd row, compared to flow paths of other rows. The maximum flow velocity magnitude in each row is 12m/sec, 11.5m/sec, 12.7m/sec, 11m/sec and 9.9m/sec for rows 1 to 5 respectively. It is the effective flow area ratios that are responsible for this behaviour as discussed before. The information regarding the maximum flow velocity magnitude variations within the trim is important for the design of the trim; in the stages where the maximum erosion rate calculations are required. It is beneficial to keep the local flow velocity magnitude within certain limits to ensure minimal erosion and for reduction in hydrodynamic losses.
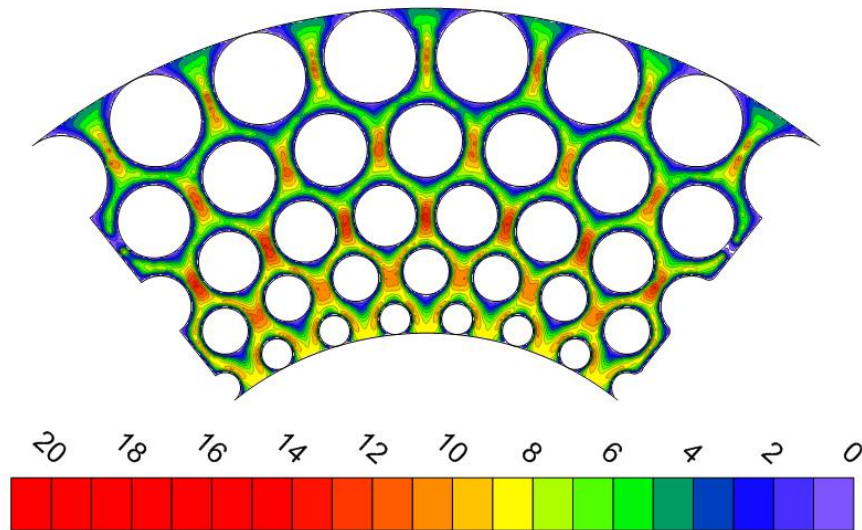
Figure 12 Flow velocity magnitude (m/sec) variations within the top disk of the trim at 100% valve opening position

In order to quantitatively analyse the flow velocity magnitude within the different flow paths of the trim, normalised velocity profiles have been drawn in each flow path, in figure 13. The geometric details of these flow paths have been represented in terms of two parameters i.e. θ and ϕ, where θ is the total circumferential dimension covered by a quarter of the disk (77° in the present study), and ϕ is the local circumferential location (as shown in figure 6(b)). Figure 13(a) depicts normalised flow velocity magnitude profiles within the flow paths of 1st, 3rd and 5th row, while figure 13(b) depicts normalised flow velocity magnitude profiles within the flow paths of 2nd and 4th rows of the top disk. This differentiation is due to the fact that there are different numbers of flow paths in different rows (rows 1, 3 and 5 have 7 flow paths, while rows 2 and 4 have 8 flow paths each). Furthermore, the flow velocity magnitude has been normalised with the maximum flow velocity within the trim, at any given valve opening position. As the maximum flow velocity magnitude of 20m/sec has been recorded in case of 10% VOP, hence, the flow velocity magnitude profiles throughout this study have been normalised against this value for effective comparison purposes.
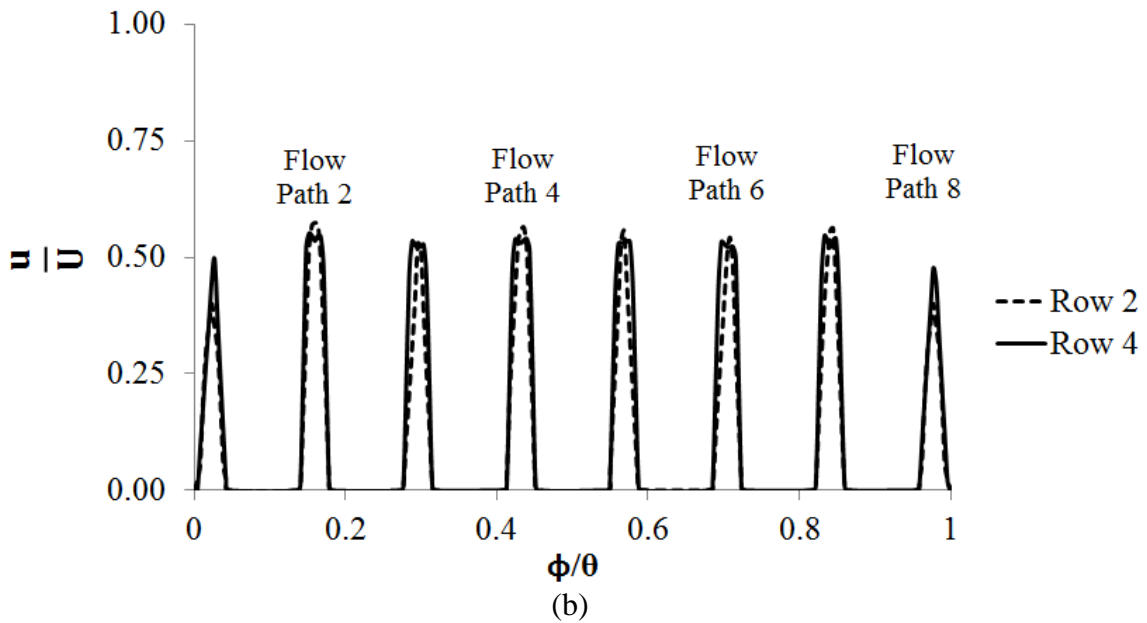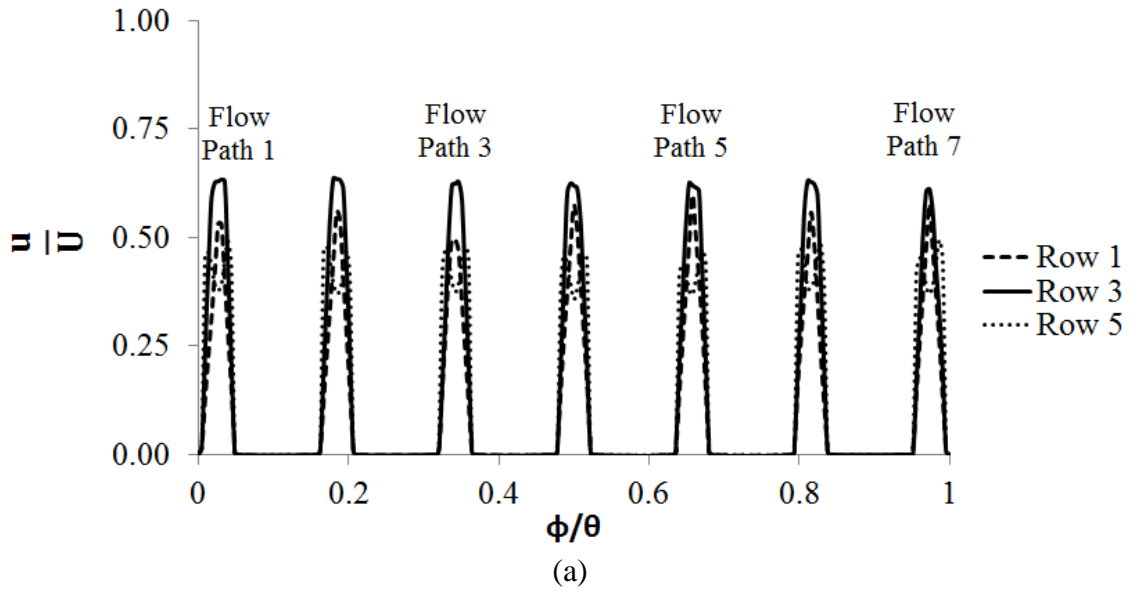
Figure 13 Normalised flow velocity magnitude profiles within different flow paths of the top disk at 100% VOP (a) for odd number of rows (b) for even number of rows

It can be seen in figures 13(a and b) that the flow velocity is maximum in the middle of the flow paths because of the wall effects on either sides, complying with no-slip boundary conditions specified to the solver. The maximum normalised flow velocity magnitudes in rows 1 to 5 are 0.6, 0.57, 0.63, 0.55 and 0.49 respectively. Hence, the global (in all the flow paths together) maximum normalised flow velocity magnitude is observed in row 3 of the trim, because of the relative flow area ratios. It can be seen that the local (in that particular flow path) maximum normalised flow velocity magnitudes decrease from rows 1 and 2 by 5%, rows 3 to 4 by 12.7%, and rows 4 to 5 by 11%, whereas it increases from row 2 to 3 by 10.5%. Hence, row 3 is contributing the most towards the hydrodynamic losses and erosion within the trim. It can be further seen that although the different velocity profiles are similar to each other, there are slight variations in the 1st and last flow paths of rows 2 and 4, in figure 13(b). The reduction in flow velocity in these flow paths is due to the geometrical configuration of these flow paths. It can be seen in figure 6 that the end flow paths of these

two rows have a straight wall at one end each, whereas, in case of rows 1, 3 and 5, both walls of the end flow paths are curved, formed by cylindrical arrays.

To estimate the contribution of various geometrical features to the global flow capacity of the trim, table 4 summarises the local flow capacities of different flow paths within the top disk of the trim at 100% VOP. It can be seen that the local flow capacity remains almost constant within the different flow paths of a particular row, although there are slight variations in the first and last flow paths of rows 2 and 4, due to wall effects as discussed earlier. It can be seen that average local flow coefficients in rows 1 to 5 are 0.275, 0.253, 0.248, 0.255 and 0.348 respectively. Hence, the local flow coefficient decreases from row 1 to 2 by 8.2% and row 2 to 3 by 2%, while it increases from row 3 to 4 by 3.1% and from row 4 to 5 by 36.5%. If the end flow paths of the 2nd and 4th rows are not considered, then the average local flow coefficients of these two rows are 0.294 and 0.295 respectively. In that case, there will be 6.7% and 1.92% increase in the average local flow capacity from row 1 to row 2 and row 3 to row 4 respectively. Hence, the estimation of local flow capacity contribution by the geometrical features of the trim to its global flow capacity is very important. It can be further seen that the 3rd row's contribution towards the global flow coefficient of the trim is the lowest, while 5th row's contribution is the highest. This further suggests that the most and the least hydrodynamic losses occur in rows 3 and 5 respectively. The local flow capacities of flow paths, of a particular row, can be summed up to give the total local flow capacity of that row, according to equation (9). Hence, the total local flow capacities of rows 1 to 5 are 1.65, 2.02, 1.73, 2.04 and 2.44 respectively.

Table 4 Local flow capacity of different flow paths of the top disk of quarter 1 at 100% VOP

	Row 1	Row 2	Row 3	Row 4	Row 5
Flow Path 1	0.277	0.127	0.249	0.131	0.350
Flow Path 2	0.277	0.297	0.250	0.304	0.349
Flow Path 3	0.271	0.298	0.249	0.290	0.346
Flow Path 4	0.273	0.301	0.246	0.300	0.344
Flow Path 5	0.280	0.285	0.244	0.290	0.338
Flow Path 6	0.278	0.287	0.244	0.296	0.346
Flow Path 7	0.272	0.295	0.251	0.291	0.365
Flow Path 8		0.130		0.139	

7.0.   Local flow capacity variations in other quarters of the disk

It is important to evaluate the local flow capacities of the rows within each of the four quarters of the disks in order to ascertain whether these quarters behave in the same manner hydrodynamically or not. Hence, the total local flow capacities of all the rows (for all the quarters of the top disk at 100% VOP) have been summarised in table 5. It can be clearly seen that Cv_{Row} remains almost constant within different quarters of the disk. However, as noticed earlier, Cv_{Row} for different rows is significantly different. Cv_{Row} of all the four quarters are summed up to estimate the total local flow capacity of that particular row. Hence, Cv_{Row} have been computed to be 7.734, 8.097, 6.942, 8.168 and 9.768 for rows 1 to 5 respectively. It can be noticed that the total local flow capacity of the 3rd row is minimum

amongst the different rows of the disk; hence row 3 is contributing the least towards the global flow capacity of the trim. This is because row 3 is offering the most resistance to the fluid flow within the trim, as compared to other rows, due to its effective flow area. The increased resistance in row 3 increases the flow velocity within this row, hence increasing trim erosion.

Table 5 Local flow capacities of all the quarters for all rows of the top disk at 100% valve opening position

		Average ΔP across all flow paths within a row	Average Q of all flow paths within a row	Cv_{Row}
		(kPa)	(m³/hr)	$\left(\sqrt{\dfrac{m^7}{kg}}\right)$
Row 1	Quarter 1	36.59	0.144	1.928
	Quarter 2	36.64	0.143	1.916
	Quarter 3	36.84	0.145	1.945
	Quarter 4	35.88	0.144	1.945
Row 2	Quarter 1	34.10	0.126	2.02
	Quarter 2	34.38	0.125	2.003
	Quarter 3	33.83	0.128	2.064
	Quarter 4	33.73	0.125	2.01
Row 3	Quarter 1	45.80	0.145	1.733
	Quarter 2	45.33	0.144	1.731
	Quarter 3	46.32	0.146	1.741
	Quarter 4	45.31	0.144	1.737
Row 4	Quarter 1	33.65	0.127	2.041
	Quarter 2	33.24	0.127	2.043
	Quarter 3	34.41	0.128	2.042
	Quarter 4	33.35	0.126	2.042
Row 5	Quarter 1	23.67	0.146	2.438
	Quarter 2	23.34	0.145	2.441
	Quarter 3	24.07	0.148	2.443
	Quarter 4	23.27	0.145	2.446

8.0. Contribution of other disks of the trim to its local flow capacity

After analysing different flow paths, rows and quarters of the top disk at 100% VOP, other disks of the trim, at the same VOP, need to be analysed in order to estimate their contribution towards the global flow coefficient of the trim. For this purpose, the middle (5th) and bottom (11th) disks have been analysed here. Figure 14 depicts the non-dimensional static pressure ratio variations, w.r.t. the top disk, within the corresponding flow paths and rows of both the middle and bottom disks of the trim It can be seen for the middle disk that the pressure ratio is almost same as the top disk upto row 3. In row 3 of the middle disk, the variations in the pressure are significantly higher than in the top disk. In the flow paths of rows 4 and 5 of the middle disk, it can be noticed that the pressure, as compared to the top disk, is less. Similarly, for the bottom disk, it is clear that there are significant differences in pressure with respect to the top disk in the corresponding flow paths and rows of the trim. The pressure drops to much lower values in case of the bottom disk, as compared to the top disk.

1
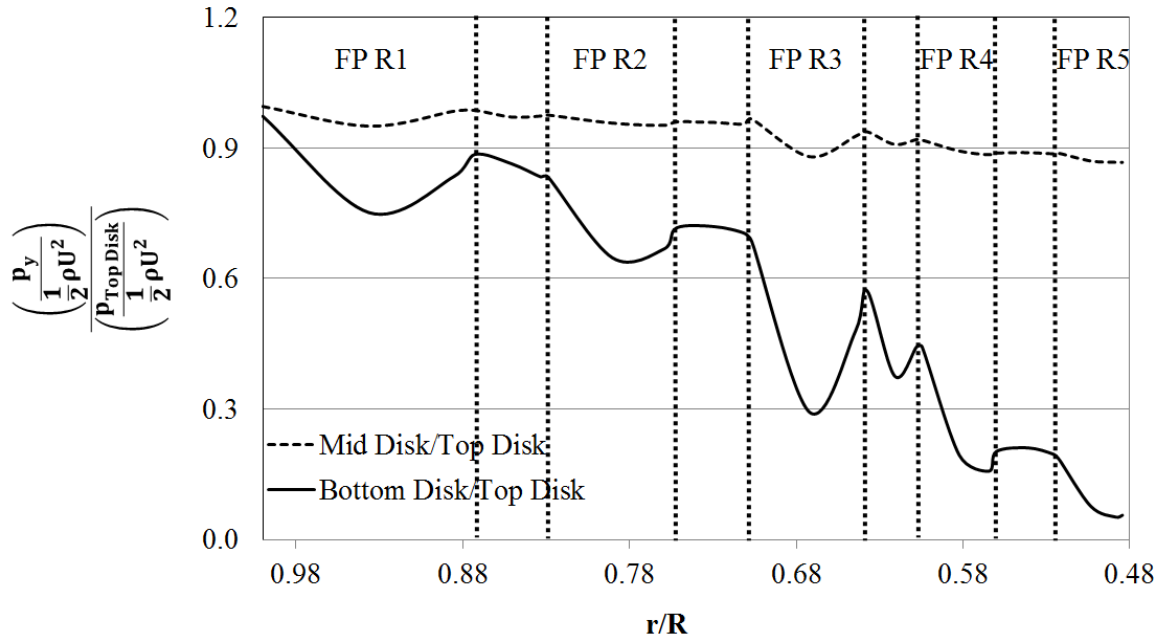
Figure 14 Normalised static gauge pressure ratio variations w.r.t. the top disk along the central flow route at 100% valve opening position

Further analysing the pressure variations within the middle and the bottom disks of the trim, figure 15 depicts the variations in non-dimensional differential static pressure ratios, w.r.t. the top disk, across the flow paths of both the middle and the bottom disks of the trim. It can be seen that the differential pressures in the middle disk are similar to the one for the top disk. However, in case of the bottom disk, the differential pressures are significantly higher than for the top disk. Moreover, it can be clearly seen that the differential pressure in row 3 of the bottom disk is substantially more than in the 3rd row of the top disk. Another important point to note over here for the bottom disk of the trim is that although it depicts lower pressure as compared to the top disk (see figure 14), the differential pressures across the flow paths of the different rows are significantly higher. Hence, it is expected that more flow is taking place through the bottom disk of the trim as compared to the top and middle disks, which is discussed in more detail later.

Normalised flow velocity magnitude profiles for the different rows and flow paths of the middle and bottom disks have been plotted in figure 16, where figures 16(a and c) corresponds to the profiles in rows 1, 3 and 5 of the middle and bottom disks respectively, while figures 16(b and d) corresponds to the profiles in rows 2 and 4 of the middle and bottom disks. It can be seen that, qualitatively, the trends are similar to the one observed in case of the top disk. However, the maximum normalised flow velocity magnitudes in different rows of the middle disk are 0.65, 0.62, 0.71, 0.6 and 0.53 respectively (from row 1 to row 5), which are 0%, 8.8%, 12.7%, 9.1% and 8.2% higher than for the top disk respectively. Similarly, the maximum normalised flow velocity magnitudes in different rows of the bottom disk are 0.84, 0.8, 0.88, 0.77 and 0.67 respectively, which are 29.2%, 40.4%, 39.7%, 40% and 36.7% higher than for the top disk respectively. In all the disks, the maximum normalised flow velocity magnitude is observed at the 3rd row, indicating maximum erosion in this row, as compared to other rows of the disk. The reason for this increase in the flow velocity magnitude is attributed to the amount of fluid flow passing through these disks.
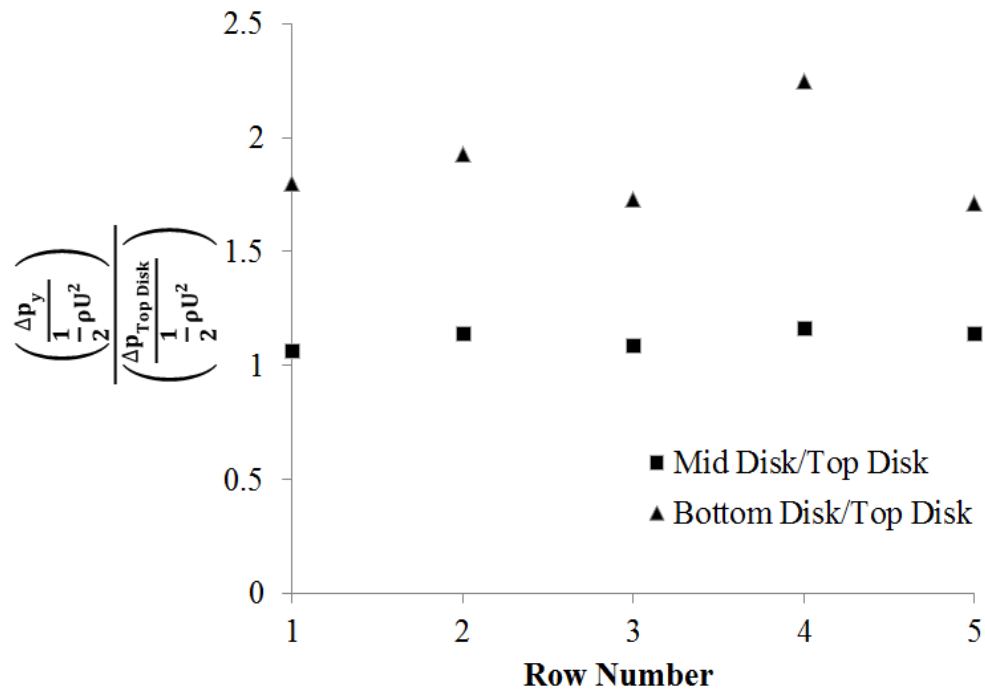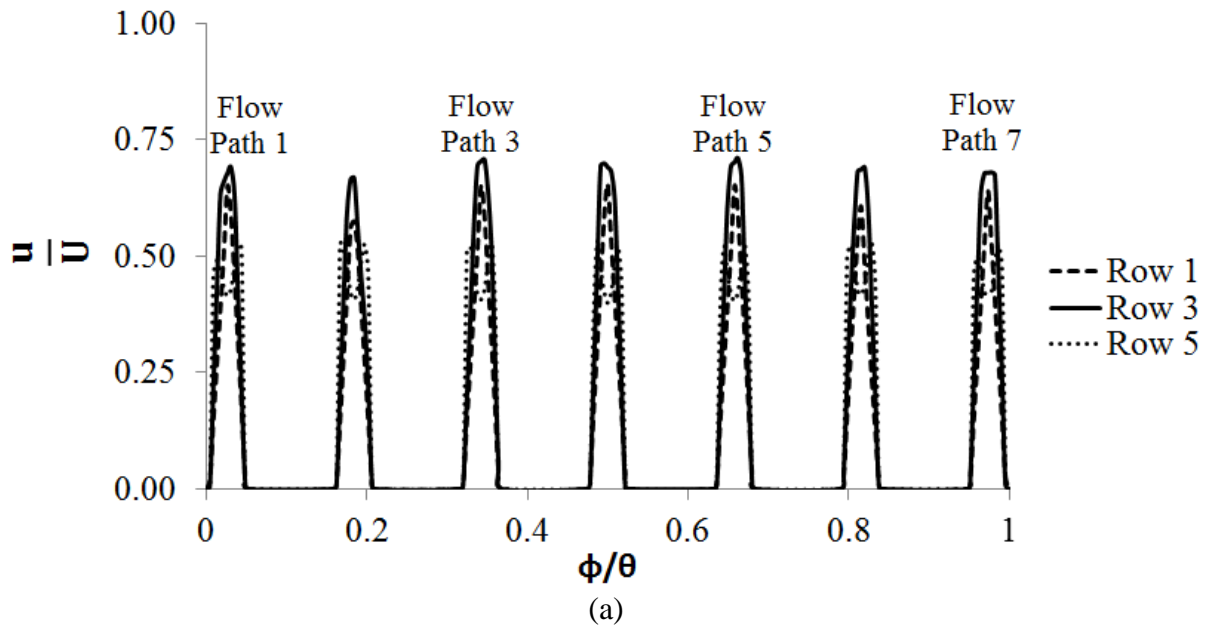
1
2 Figure 15 Normalised differential static gauge pressure ratio variations w.r.t. the top disk in
3   various rows of the trim along the central flow route at 100% valve opening position
4
5

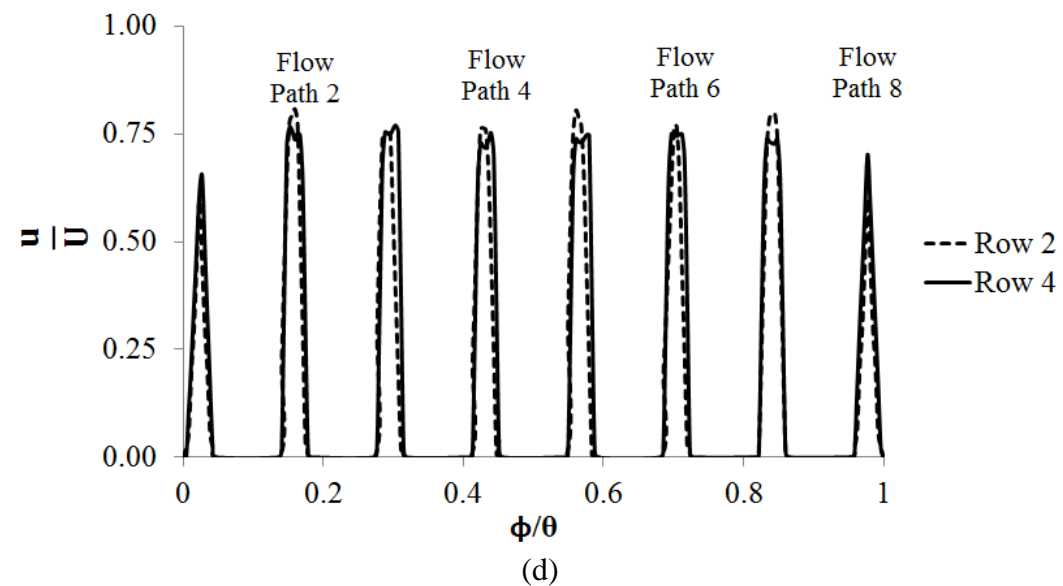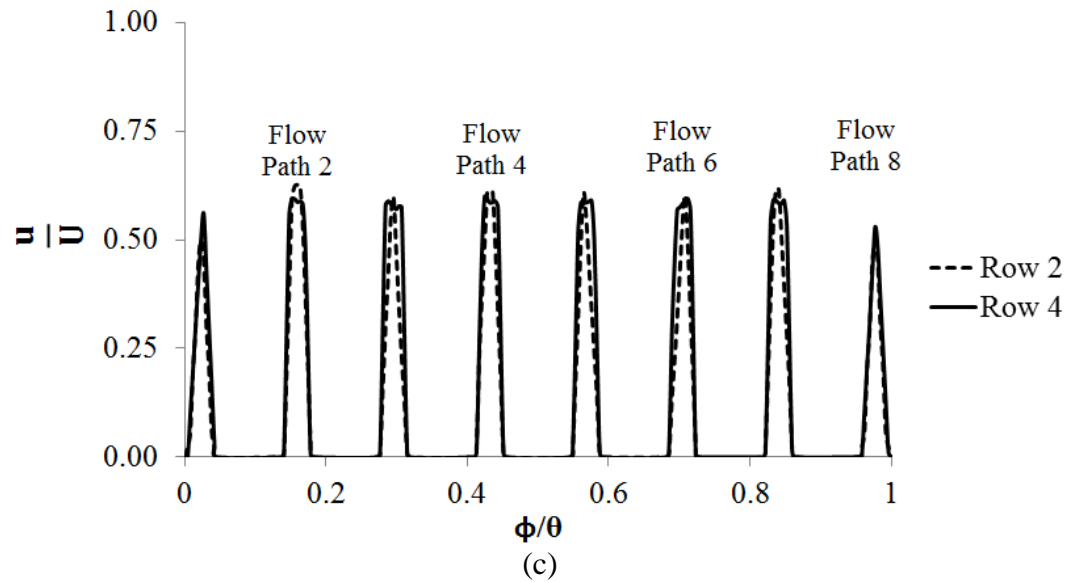
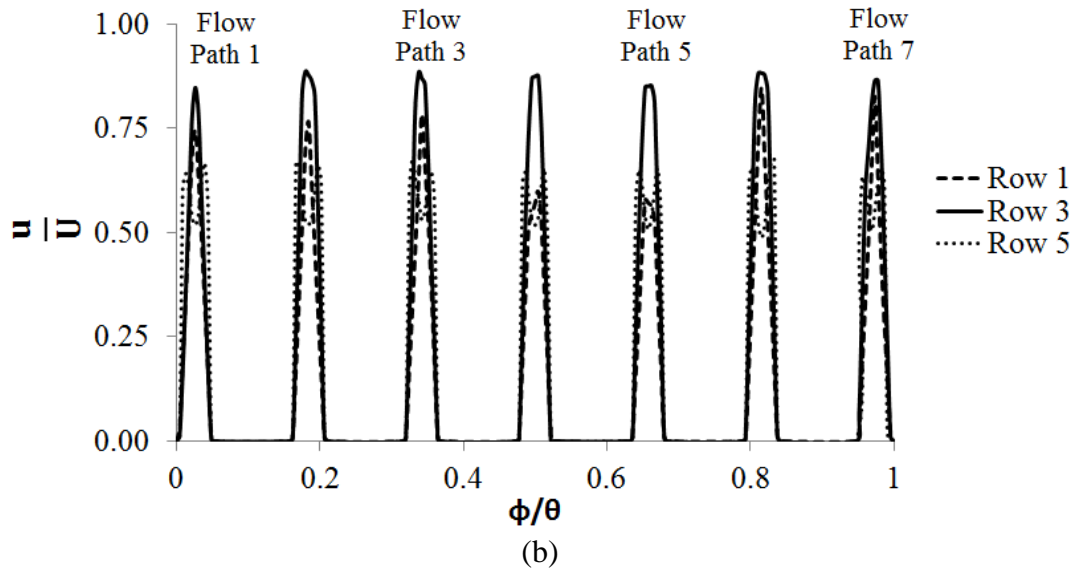
6
7   (a)

Figure 16 Normalised flow velocity magnitude profiles at 100% VOP within different flow paths of (a) middle disk for odd number of rows (b) bottom disk for odd number of rows (c) middle disk for even number of rows (d) bottom disk for even number of rows

Quantitatively analysing the reason for higher differential pressures and flow velocity in the middle and bottom disks of the trim, as compared to the top disk, table 6 summarises the mass flow rate of water entering the trim through the various flow paths of the first (outermost) row for the top, middle and bottom disks. It can be clearly seen that the amount of fluid passing through the middle and bottom disks is higher than for the top disk. It is noteworthy that, on average, the amount of flow taking place through the middle disk is 6.4% higher than the top disk, while it is 40% higher for the bottom disk. It suggests that the middle disk offers less resistance to the flow of fluid as compared to the top row, while the flow resistance is further reduced in case of the bottom disk. The effect this has on the flow distribution within the trim is shown in terms of flow streamlines in figure 17. It can be seen that the number of streamlines (amount of fluid flow) passing through the different disks of the trim increases from the top to the bottom disks, due to the wall effects.

Table 6 Mass flow rate passing through the 1st row of top, middle and bottom disks of the trim at 100% VOP

	Mass Flow Rate (kg/sec)		
	Top Disk	Middle Disk	Bottom Disk
Flow Path 1	0.0392	0.0408	0.0536
Flow Path 2	0.0407	0.0437	0.0557
Flow Path 3	0.0402	0.0418	0.0554
Flow Path 4	0.0410	0.0432	0.0579
Flow Path 5	0.0405	0.0433	0.0577
Flow Path 6	0.0395	0.0421	0.0569
Flow Path 7	0.0385	0.0427	0.0543
Average	0.0399	0.0425	0.0559
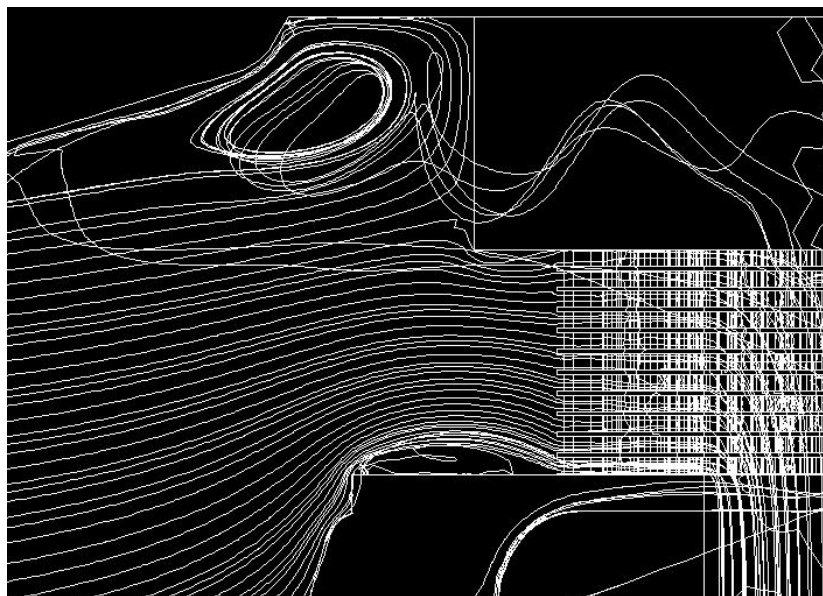
Figure 17 Streamlines passing through different disks of the trim at 100% VOP

9.0. Effect of valve opening position on the flow capacity of the trim

After carrying out detailed investigations in to the non-dimensional pressure and velocity magnitude, and the local flow capacity of the different flow paths, rows, quarters and disks of the trim, the next step is to estimate the effects of the valve opening position on the contribution to local flow capacity of the trim by the various geometrical features. For this purpose, VOP of 60% and 10% have been considered in this section, and comparisons have been made against 100% VOP wherever applicable. This analysis is important as the flow distribution amongst the disks may change by changing the VOP, affecting the local flow capacity of the disks and the global flow capacity of the trim.

Figure 18 depicts the non-dimensional static pressure ratio variations at various valve opening positions, w.r.t. 100% VOP, within the corresponding flow paths and rows of the top disk of the trim It can be seen for 60% that the pressure ratio is almost the same as for 100% VOP in row 1 of the trim. From row 2 onwards, the variations in the pressure are significantly higher than for 100% VOP; the pressure keeps on decreasing. It can also be noticed that pressure decrease in row 3 of the disk is substantially more at 60% VOP as compared to 100% VOP. Similarly, for 40% and 10% VOPs, it is clear that there are significant differences in pressure with respect to 100% VOP in the corresponding flow paths and rows of the trim. The pressure drops to much lower values, especially in row 3, in case of both 40% and 10% VOPs, as compared to 100% VOP.
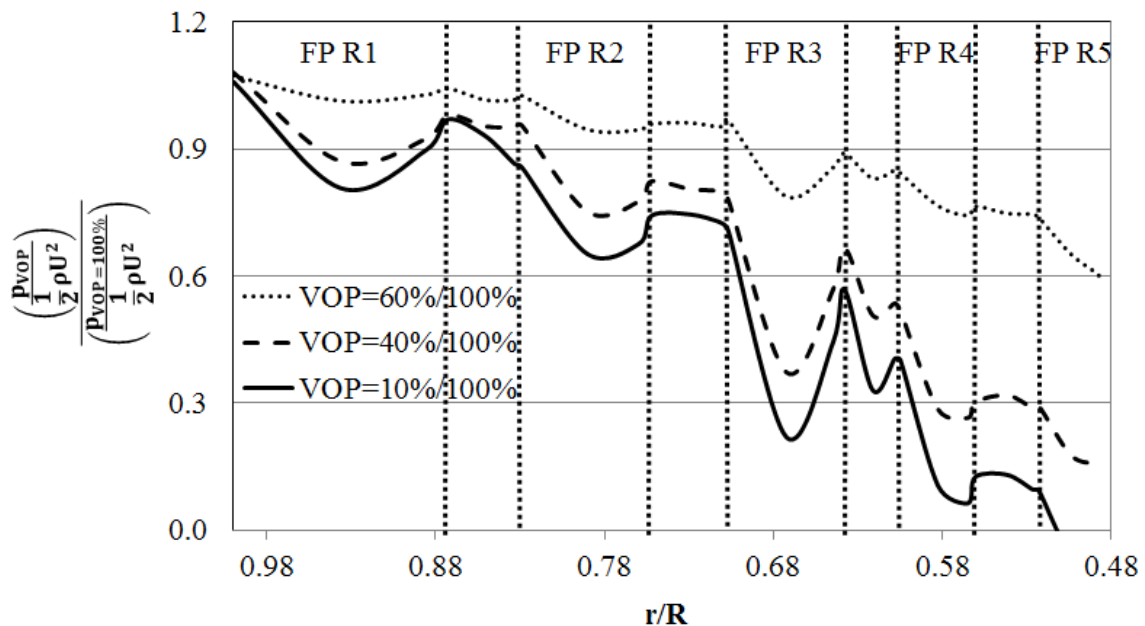

Figure 18 Normalised static gauge pressure ratio variations w.r.t. 100% VOP along the central flow route of the top disk of the trim

Further analysing the pressure variations at different VOPs, figure 19 depicts the variations in non-dimensional differential static pressure ratios, w.r.t. 100% VOP, across the flow paths of different rows of the trim. It can be seen that the differential pressures at all 60%, 40% and 10% VOPs are significantly higher than for at 100% VOP. It can also be seen that the differential pressure at 10% VOP is higher than at 40%, while the differential pressure at 40% VOP is higher than at 60% VOP. Furthermore, in the 3rd row of the disk, the differential pressure is substantially higher than at 100% VOP, indicating increased hydrodynamic losses in row 3 of the trim.
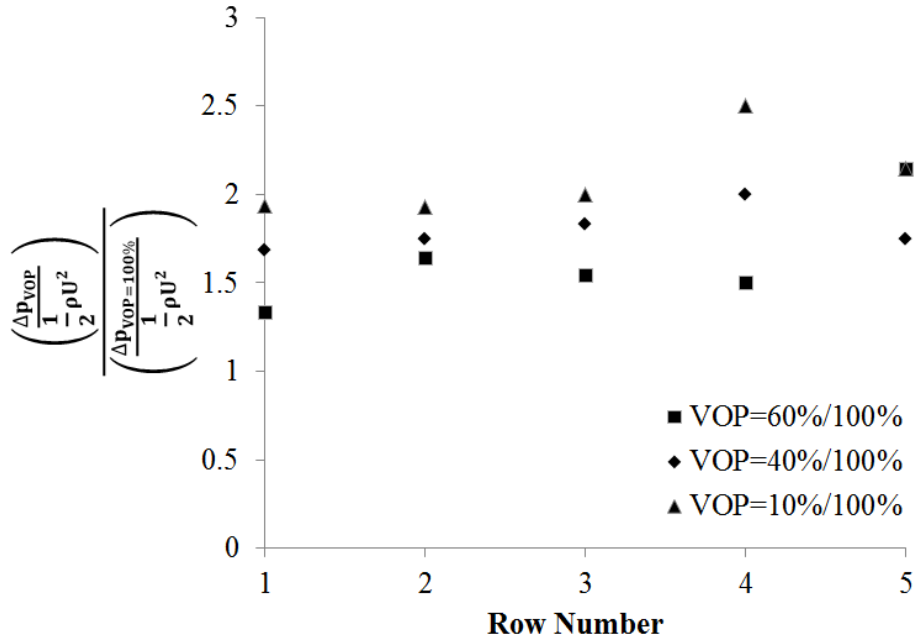
Figure 19 Normalised differential static gauge pressure ratio variations w.r.t. 100% VOP in various rows of the trim along the central flow route of the top disk of the trim

Normalised flow velocity magnitude profiles for the different rows and flow paths at 10%, 60% and 100% VOPs have been plotted in figure 16, where figures 20(a and c) corresponds to the profiles in rows 1, 3 and 5 at 60% and 10% VOPs respectively, while figures 20(b and d) corresponds to the profiles in rows 2 and 4 at 60% and 10% VOPs. The maximum normalised flow velocity magnitudes in different rows at 60% and 10% VOPs are 0.71, 0.68, 0.76, 0.64, 0.61 and 0.65, 0.43, 0.66, 0.32 and 0.13 respectively. These are (for 60% VOP) 18.3%, 19.3%, 20.6%, 16.4% and 24.5% higher than for 100% VOP respectively. Similarly, the maximum normalised flow velocity magnitudes in different rows at 10% VOP are 8.3% higher, 24.6% lower, 4.8% higher, 41.8% lower and 73.5% lower respectively, as compared to 100% VOP. At all VOPs, the maximum normalised flow velocity magnitude is observed at the 3rd row, indicating maximum erosion in this row. The reason for this increase in the flow velocity magnitude is the amount of fluid flow passing through these rows at different VOPs.
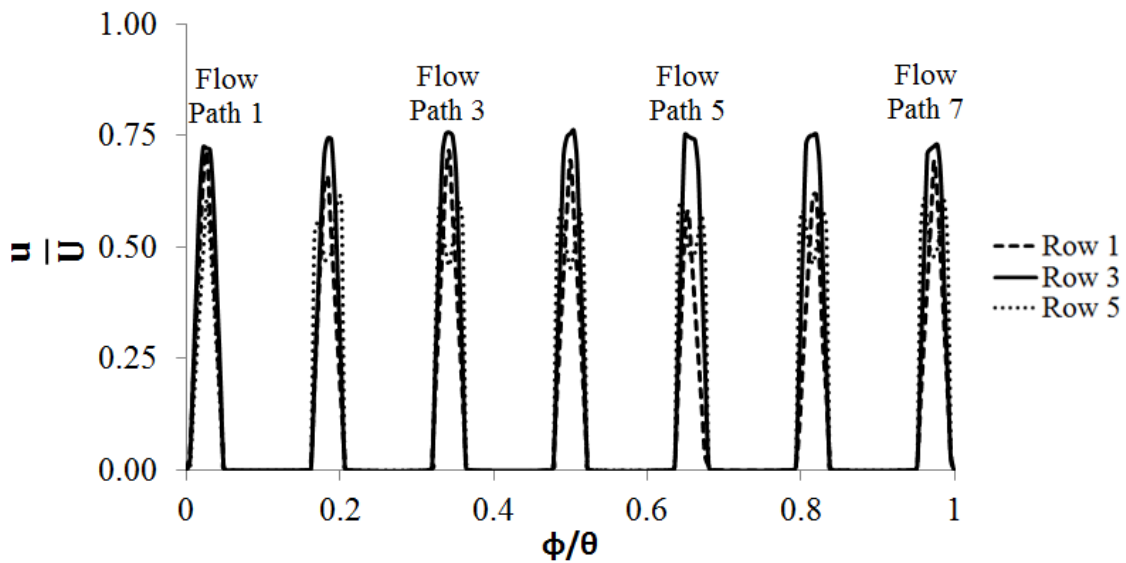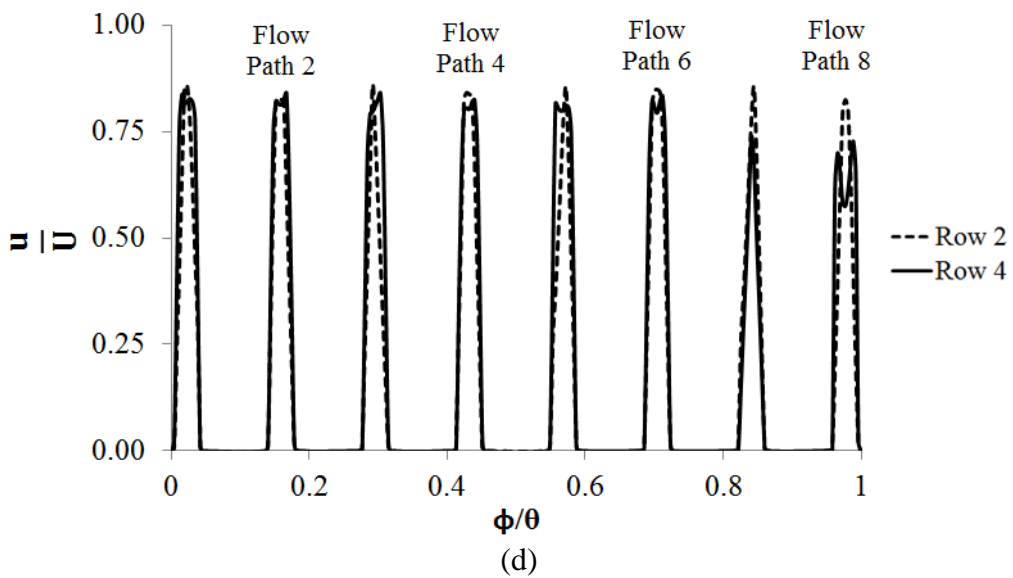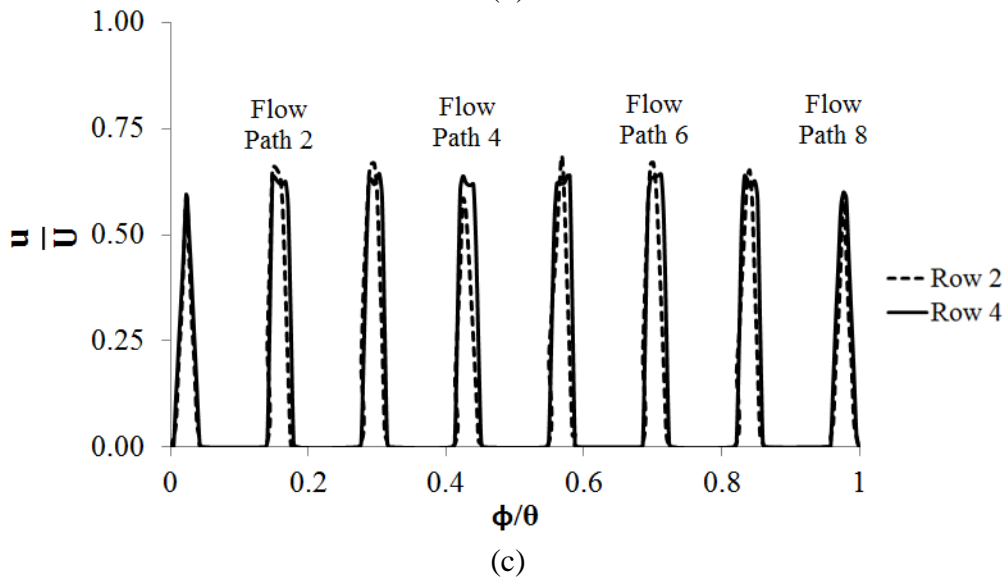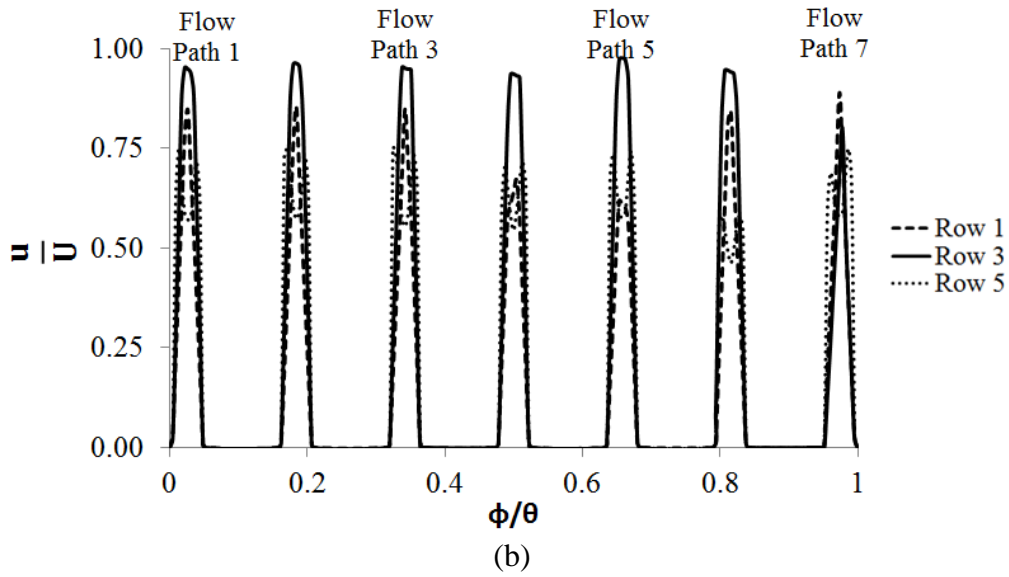

(a)

Figure 20 Normalised flow velocity magnitude profiles within different flow paths of the top disk at (a) 60% VOP for odd number of rows (b) 10% VOP for odd number of rows (c) 60% VOP for even number of rows (d) 10% VOP for even number of rows

Based on the results presented in this study regarding the local flow capacity at a given location within the trim (flow paths, rows, disks and at different valve opening positions), and using advance statistical tools such as multiple variable regression analysis, a semi-empirical local Cv prediction model i.e. $Cv_{Flow-Path}$ in equation (10) has been developed and compared against the measured local flow capacity of the trim. This prediction model is presented in equation (12), which shows the local flow capacity of a flow path as a function of the valve opening position (VOP), disk number of the trim, row number of the disk and flow path number of the row. Volumetric flow rate (Q) and the differential pressure (ΔP) used to develop this predicted model are taken from table 1, which are measured experimentally. It can be seen that as the valve opening position increases (from 0.1 to 1), local Cv decreases. Substituting equation (12) in equation (10), as the VOP increases, Cv_{Trim} also increases. Furthermore, it can be seen that as the disk number increases i.e. going from the bottom disk to top disk, local Cv decreases. Moreover, increase in row number i.e. from outer (bigger cylinders) to inner (smaller cylinders), local Cv increases. Equation (12) can be substituted in equation (10) to predict the global/total flow capacity of the trim, where all the inputs are known in advance (Row, VOP, Disk and FP), or can be measured experimentally (Q and ΔP). Figure 21 depicts a comparison between CFD measured and equation (12) predicted local flow capacities. It can be seen that more than 90% of the data lies within ±20% band. Hence, equation (12) can be used to determine the local flow capacity of the trim with reasonable accuracy.

$$Cv_{Flow-Path} = \frac{0.57Q(Row+1)^{0.11}(FP+1)^{0.01}}{\sqrt{\Delta P}(VOP+1)^{2.78}(Disk+1)^{0.025}} \tag{12}$$
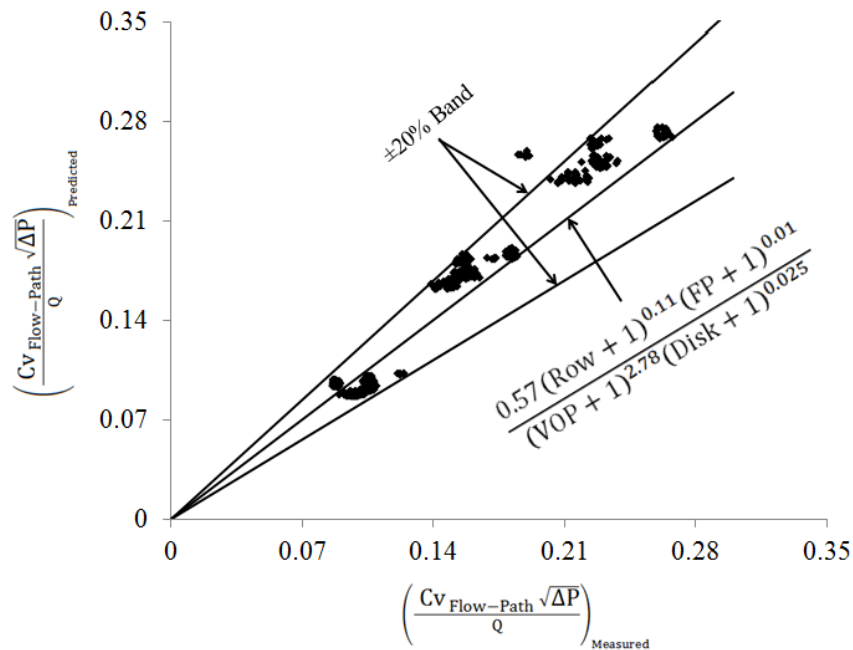

Figure 21 Comparison between measured and predicted normalised $Cv_{Flow-Paths}$

10.0. Conclusions

Severe service control valves are typically installed with geometrically complex trims to control the flow in varies energy systems. The flow capacity of these trims is one of the most important parameters that dictate the effectiveness of the trims, and hence, the effectiveness of the energy systems. The global flow capacity of a geometrically complex trim has been measured experimentally in the present study. The results indicate that as the valve opening

position increases, the global flow capacity of the trim increases. This increase in the global flow capacity of the trim is due to the fact that for the same differential pressure across the control valve system, the mass flow rate of the fluid decreases, increasing the flow capacity. The decrease in the mass flow rate is a direct consequence of the decrease in the valve opening position, offering more resistance to the flow.

The current study uniquely relates the local flow capacity, and hence, the local flow features, with the global flow capacity of the trim. The predicted results indicate that the local capacity within different flow paths of a particular row of the trim remains the same, while it changes from one row to another. It has been noticed that the 3rd row of the trim demonstrates the lowest flow capacity, but highest pressure drop and flow velocity, resulting in severe losses and erosion within the trim. Furthermore, it has also been shown that different disks of a trim have different flow capacities, and as the valve opening position increases, the flow capacity of the trim also increases. Based on the global experimental results, and the local numerical predictions, a prediction model has been developed that inter-relates the geometrical features of a trim to its local flow capacity, as the geometrical features dictate the flow capacity of the trim. This prediction model is expected to be a useful tool for trim designers in order to design more efficient trims. Moreover, this prediction model can be integrated with the design tool, for the energy systems, for integrated performance estimation.

Nomenclature

Q	Volumetric flow rate (m^3/hr)
D	Diameter (m)
p	Static gauge pressure (Pa)
ρ	Density of the fluid (kg/m^3)
ρ_o	Operating Density (kg/m^3)
ΔP	Differential pressure across the valve (kPa)
VOP	Valve Opening Position (%)
Cv	Flow Capacity $\left(\sqrt{m^7/kg}\right)$
N_1	Numerical constant (-)
F_R	Reynolds number factor (-)
F_P	Piping geometry factor (-)
U	Flow velocity magnitude (m/sec)

References

[1]   S. K. Kang, J. Y. Yoon, S. H. Kang and B. H. Lee (2006) Numerical and experimental investigations on backward fitting effect on valve flow coefficient, IMechE Part E: Journal of Process Mechanical Engineering, 220, 217 – 220

[2]   A. Beune, J. G. M. Kuerten and J. Schmiddlet (2011) Numerical calculation and experimental validation of a safety valve flows at pressures up to 600bar, AIChE: Fluid Mechanics and Transport Phenomena, 57, 3285 – 3298

[3]   F. Lin and G. A. Schohl (2004) CFD prediction and validation of butterfly valve hydrodynamic forces, Proceedings of World Water and Environmental Resources Congress, Salt Lake City, U.S.A.

[4]   Q. Yang, Z. Zhang, M. Liu and J. Hu (2011) Numerical simulation of fluid flow inside the valve, Procedia Engineering, 23, 543 – 550

[5]   Y. J. An, B. J. Kim and B. R. Shin (2008) Numerical analysis of 3-D flow through LNG marine control valves for their advanced design, Journal of Mechanical Science and Technology, 22, 1998 – 2005

[6]   A. Grace and P. Frawley (2011) Experimental parametric equation for the prediction of valve coefficient (Cv) for choke valve trims, International Journal of Pressure Vessels and Piping, 88, 109 – 1148

[7]   BS EN 60534-2-1 (2011) Industrial-process control valves. Part 2-1: Flow capacity – Sizing equations for fluid flow under installed conditions

[8]   X. G. Li, D. X. Liu, S, M. Xu and H. Li (2009) CFD simulation of hydrodynamics of valve tray, Chemical Engineering and Processing, 48, 145 – 151

[9]   D. Wu, S. Li and P. Wu (2015) CFD simulation of flow-pressure characteristics of a pressure control valve for automotive fuel supply system, Energy Conversion and Management, 101, 658 – 665

[10]   J. Qian, L. Wei, Z. Jin, J. Wang, H. Zhang and A. Lu (2014) CFD analysis on the dynamic flow characteristics of the pilot-control globe valve, Energy Conversion and Management, 87, 220 – 226

[11]   J. R. Valdes, M. J. Miana, J. L. Nunez and T. Putz (2008) Reduced order model for estimation of fluid flow and flow forces in hydraulic proportional valves, Energy Conversion and Management, 49, 1517 – 1529

[12]   C. Srikanth and C. Bhasker (2009) Flow analysis in valve with moving grids through CFD techniques, Advances in Engineering Software, 40, 193 – 201

[13]   R. Amirante, G. D. Vescovo and A. Lippolis (2006) Flow forces analysis of an open center hydraulic directional control valve sliding spool, Energy Conversion and Management, 47, 114 – 131

[14]   R. Amirante, P. G. Moscatelli and L. A. Catalano (2007) Evaluation of the flow forces on a direct (single stage) proportional valve by means of a computational fluid dynamic analysis, Energy Conversion and Management, 48, 942 – 953

[15]   R. Amirante, G. D. Vescovo and A. Lippolis (2006) Evaluation of the flow forces on an open centre directional control valve by means of a computational fluid dynamic analysis, Energy Conversion and Management, 47, 1748 – 1760

[16]   E. Lisowski, J. Rajda (2013) CFD analysis of pressure loss during flow by hydraulic directional control valve constructed from logic valves, Energy Conversion and Management, 65, 285 – 291

[17]   E. Lisowski, W. Czyzycki, J. Rajda (2014) Multifunctional four-port directional control valve constructed from logic valves, Energy Conversion and Management, 87, 905 – 913

[18]   E. Lisowski, G. Filo (2016) CFD analysis of the characteristics of a proportional flow control valve with an innovative opening shape, Energy Conversion and Management, 123, 15 – 28

[19]   Weir Valves and Controls UK Ltd. https://www.global.weir/products/product-catalogue/blakeborough-bv500-globe-control-valve-and-bv501-angle-control-valve

[20]   BS EN 60534-2-3 (1998) Industrial-process control valves. Part 2-3: Flow capacity – Test procedures

[21]   Taimoor Asim (2013) Report submitted to Weir Valves and Controls, U.K.

[22]   BS EN 60534-2-5 (2003) Industrial-process control valves. Part 2-5: Flow capacity – Sizing equations for fluid flow through multistage control valves with interstage recovery

[23]   S. Y. Jeon, J. Y. Yoon and M. S. Shin (2010) Flow characteristics and performance evaluation of butterfly valves using numerical analysis, Institute of Physics Conference Series: Earth and Environmental Science, 12, 012099

[24]   X. G. Song and Y. C. Park (2007) Numerical analysis of butterfly valve-prediction of flow coefficient and hydrodynamic torque coefficient, Proceedings of the World Congress on Engineering and Computer Science, San Francisco, U.S.A.

[25]   R. Mishra, E. Palmer and J. Fieldhouse (2009) An Optimization Study of a Multiple-Row Pin-Vented Brake Disc to Promote Brake Cooling Using Computational Fluid Dynamics, Proceedings of the Institution of Mechanical Engineers, Part D: Journal of Automobile Engineering, 223, 865–875

[26]   Taimoor Asim, Rakesh Mishra, Matthew Charlton and Antonio Oliveira (2015) Capacity Testing and Local Flow Analysis of Geometrically Complex Trims Installed within a Commercial Control Valve, International Conference of Jets, Wakes and Separated Flows, June 15-18, Stockholm, Sweden

[27]   James Green, Rakesh Mishra, Matthew Charlton and Owen (2012) Validation of CFD predictions using process data obtained from flow through an industrial control valve, Journal of Physics: Conference Series, 364, 012074

[28]   James Green, and Rakesh Mishra, Matthew Charlton and Owen (2012) Local Analysis of Flow Conditions within a Geometrically Complex Control Valve Trim using CFD, Journal of Physics: Conference Series, 364, 012075

[29]   R. Mishra, S. N. Singh and V. Seshedri (1998) Study of Wear Characteristics and Solid Distribution in Constant Area and Erosion-Resistant Long-Radius Pipe Bends for the flow of Multisized Particulate Slurries, Wear, 217, 297–306

[30]   R. Mishra, S. N. Singh and V. Seshadri (1998) Velocity measurement in solid-liquid flows using an impact probe, Flow Measurement and Instrumentation, 8, 157–165

[31]   R. Mishra, S. N. Singh and V. Seshadri (1998) Improved model for the prediction of pressure drop and velocity field in multi-sized particulate slurry flow through horizontal pipes, Powder Handling and Processing, 10, 279–287.

[32]   Agarwal, V. C. Mishra, R. (1998) Optimal Design of a Multi-Stage Capsule Handling Multi-Phase Pipeline, International Journal of Pressure Vessels and Piping, 75, 27 – 35.

[33]   H. K. Versteeg and W. Malalasekera (1995) An Introduction to Computational Fluid Dynamics, Longman Scientific and Technical, U.K., ISBN: 0131274988

[34]   T. Cebeci, J. P. Shao, F. Kafyeke and E. Laurendeau (2005) Computational Fluid Dynamics for Engineers, Horizons Publishing, U.S.A., ISBN: 3540244514

[35]   H. Lomax, T. H. Pulliam and D. W. Zingg (2001) Fundamentals of Computational Fluid Dynamics, Springer, ISBN: 3540416072

[36]   Karen Morton (2003) Optimisation of a high-energy loss control valve trim using computational and experimental techniques, Ph.D. Thesis, University of Manchester, U.K.

[37]   Taimoor Asim (2013) Computational Fluid Dynamics based Diagnostics and Optimal Design of Hydraulic Capsule Pipelines, Ph.D. Thesis, University of Huddersfield, U.K.

[38]   Taimoor Asim and Rakesh Mishra (2016) Optimal Design of Hydraulic Capsule Pipeline Transporting Spherical Capsules, The Canadian Journal of Chemical Engineering, 94, 966 – 979

[39]   Taimoor Asim and Rakesh Mishra (2016) Computational Fluid Dynamics based Optimal Design of Hydraulic Capsule Pipelines Transporting Cylindrical Capsules, International Journal of Powder Technology, 295, 180 – 201

[40]   Taimoor Asim, Rakesh Mishra, Sufyan Abushaala and Anuj Jain (2016) Development of a Design Methodology for Hydraulic Pipelines carrying Rectangular Capsules, International Journal of Pressure Vessels and Piping, 146, 111 – 128